

## Original Research Article



# Nilotinib restores memory function by preventing dopaminergic neuron degeneration in a mouse model of Alzheimer's Disease

Livia La Barbera<sup>a,b,1</sup>, Francescangelo Vedele<sup>b,c,1</sup>, Annalisa Nobili<sup>a,b,1</sup>, Paraskevi Krashia<sup>a,b,\*</sup>, Elena Spoletti<sup>a</sup>, Emanuele Claudio Latagliata<sup>b</sup>, Debora Cutuli<sup>b,d</sup>, Emma Cauzzi<sup>a,e</sup>, Ramona Marino<sup>a</sup>, Maria Teresa Viscomi<sup>b,f</sup>, Laura Petrosini<sup>b</sup>, Stefano Puglisi-Allegra<sup>g</sup>, Marcello Melone<sup>h,i</sup>, Flavio Keller<sup>a</sup>, Nicola Biagio Mercuri<sup>b,c</sup>, Fiorenzo Conti<sup>h,i,j</sup>, Marcello D'Amelio<sup>a,b,\*</sup>

<sup>a</sup> Department of Medicine and Surgery, Department of Sciences and Technologies for Humans and Environment, University Campus Bio-Medico, 00128, Rome, Italy

<sup>b</sup> Department of Experimental Neurosciences, IRCCS Santa Lucia Foundation, 00143, Rome, Italy

<sup>c</sup> Department of Systems Medicine, University of Rome Tor Vergata, 00133, Rome, Italy

<sup>d</sup> Department of Psychology, Sapienza University of Rome, 00185, Rome, Italy

<sup>e</sup> School of Medicine and Surgery, University of Milano-Bicocca, Monza, Italy

<sup>f</sup> Department of Life Science and Public Health Section of Histology and Embryology, Università Cattolica del Sacro Cuore, 00168, Rome, Italy

<sup>g</sup> IRCCS Neuromed, 86077, Pozzilli, Italy

<sup>h</sup> Section of Neuroscience and Cell Biology, Department of Experimental and Clinical Medicine, Università Politecnica delle Marche (UNIVPM), 60020, Ancona, Italy

<sup>i</sup> Center for Neurobiology of Aging, IRCCS Istituto Nazionale Ricovero e Cura Anziani (INRCA), 60020, Ancona, Italy

<sup>j</sup> Foundation for Molecular Medicine, Università Politecnica delle Marche, 60020, Ancona, Italy

## ARTICLE INFO

## Keywords:

Ventral Tegmental Area

Autophagy

Midbrain

Tg2576

Tyrosine kinase

## ABSTRACT

What happens precociously to the brain destined to develop Alzheimer's Disease (AD) still remains to be elucidated and this is one reason why effective AD treatments are missing. Recent experimental and clinical studies indicate that the degeneration of the dopaminergic (DA) neurons in the Ventral Tegmental Area (VTA) could be one of the first events occurring in AD. However, the causes of the increased vulnerability of DA neurons in AD are missing.

Here, we deeply investigate the physiology of DA neurons in the VTA before, at the onset, and after onset of VTA neurodegeneration. We use the Tg2576 mouse model of AD, overexpressing a mutated form of the human APP, to identify molecular targets that can be manipulated pharmacologically. We show that in Tg2576 mice, DA neurons of the VTA at the onset of degeneration undergo slight but functionally relevant changes in their electrophysiological properties and cell morphology. Importantly, these changes are associated with accumulation of autophagosomes, suggestive of a dysfunctional autophagy, and with enhanced activation of c-Abl, a tyrosine kinase previously implicated in the pathogenesis of neurodegenerative diseases.

Chronic treatment of Tg2576 mice with Nilotinib, a validated c-Abl inhibitor, reduces c-Abl phosphorylation, improves autophagy, reduces A $\beta$  levels and – more importantly – prevents degeneration as well as functional and morphological alterations in DA neurons of the VTA. Interestingly, the drug prevents the reduction of DA outflow to the hippocampus and ameliorates hippocampal-related cognitive functions.

Our results strive to identify early pathological brain changes in AD, to provide a rational basis for new therapeutic interventions able to slow down the disease progression.

\* Corresponding authors at: Department of Medicine and Surgery, Department of Sciences and Technologies for Humans and Environment, University Campus Bio-Medico, 00128, Rome, Italy.

E-mail addresses: [k.paraskevi@unicampus.it](mailto:k.paraskevi@unicampus.it) (P. Krashia), [m.damelio@unicampus.it](mailto:m.damelio@unicampus.it) (M. D'Amelio).

<sup>1</sup> These authors contributed equally.

## 1. Introduction

Alzheimer's disease (AD) is a neurodegenerative disorder with a slow progression and devastating outcomes. AD is characterized by a gradual loss of memory and cognition (D'Amelio and Rossini, 2012) and by comorbidities such as epilepsy, sleep disorders, and neuropsychiatric symptoms like apathy, anxiety, depression and aggressivity (Alves et al., 2017; Ismail et al., 2016; Lyketsos et al., 2011; Masters et al., 2015; Musiek et al., 2018; Noebels, 2011). The main neuropathological hallmarks of AD are extracellular amyloid  $\beta$  ( $A\beta$ ) deposits, intracellular neurofibrillary tangles, inflammation, neuronal dysfunction, and brain atrophy. The classical amyloid hypothesis, which states that the accumulation and deposition of oligomeric or fibrillar  $A\beta$  peptides are the primary cause of AD, has been the most widespread theory in the medical and scientific community for over 20 years (Ch  telat, 2013; Hardy and Selkoe, 2002; Herrup, 2015; Tanzi and Bertram, 2005). However, all attempts to develop  $A\beta$ -targeting drugs to reverse deficits in memory and cognition have ended in failure, despite being successful in reducing the  $A\beta$  load (Canter et al., 2016; Huang et al., 2020).

In the last years, increasing evidence has underlined the importance of dopamine (DA) in the progression of AD. In compliance with its importance for hippocampal-dependent memory performances (Bethus et al., 2010; Broussard et al., 2016; Lisman and Grace, 2005; McNamara et al., 2014; Rosen et al., 2015; Rossato et al., 2009; Yang et al., 2017), it was not surprising that multiple studies established an early link between AD and deficits in mesocorticolimbic DA signalling (Allard et al., 1990; Costa et al., 2016; Gibb et al., 1989; Joyce et al., 1997; Kempainen et al., 2003; Koch et al., 2014; Kumar and Patel, 2007; Murray et al., 1995; Rinne et al., 1986a, 1986b; Storga et al., 1996). Notably, several dopaminergic drugs may help reduce temporarily some symptoms in AD patients, thus ameliorating the quality of life (Koch et al., 2020, 2014, 2011; Martorana and Koch, 2014; Monteverde et al., 1990). More importantly, in the context of this research paper, the increase of DA drive – evoked by dopaminergic drugs or stimulation of the dopaminergic neurotransmission – improves synaptic plasticity dysfunctions, cognitive impairment and memory deficits in different experimental models of AD (Ambr  e et al., 2009; Guzm  n-Ramos et al., 2012; Hao et al., 2015; Himeno et al., 2011; J  rgensen et al., 2011; Pazini et al., 2013; Tsunekawa et al., 2008). This evidence supports the notion that the mesocorticolimbic DA system undergoes profound changes since the early phases of the disease (Martorana and Koch, 2014).

In line with this concept, we have recently reported an early, progressive, and selective loss of the Ventral Tegmental Area (VTA) DA neurons in the Tg2576 mouse model of familial AD, long before  $A\beta$  plaque deposition (Nobili et al., 2017). The VTA is a deep brainstem nucleus containing DA neurons that project diffusively to the prefrontal cortex, hippocampus, nucleus accumbens (NAc), olfactory bulb, and amygdala (Bj  rklund and Dunnett, 2007; Gasbarri et al., 1994). In the Tg2576 mouse model, the degeneration of DA neurons results in a lower DA outflow to the projection areas, including the hippocampus and NAc shell, and correlates with the impairment of the VTA-hippocampus-NAc circuit and with deficits in memory and reward performances (Cordella et al., 2018; Nobili et al., 2017). In line with our data obtained in Tg2576 mice, loss of neurons that contain tyrosine-hydroxylase (TH), the rate-limiting enzyme of catecholamine biosynthesis, has also been observed in two other commonly-used AD models, the 3 $\times$ Tg-AD and APPsw/PS1 $\Delta$ E9 mice (Liu et al., 2008; Moreno-Castilla et al., 2016). Importantly, the observations in Tg2576 mice led to several independent clinical studies focused on the alterations occurring in the VTA of mild-cognitive impairment (MCI) and AD patients. In particular, these works pinpoint the functional, structural and metabolic changes affecting the VTA and its projection areas in the mesocorticolimbic pathway since the early stages of the disease (Caligiore et al., 2020; D'Amelio et al., 2018b; De Marco and Venneri, 2018; Iaccarino et al., 2020; Serra et al., 2018), and highlighted the VTA volume or connectivity alterations as prodromal clinical markers to predict conversion

from a healthy state to clinical AD (D'Amelio et al., 2018a; Venneri and De Marco, 2020).

Despite these clinical advances, however, the causes of the increased vulnerability of VTA DA neurons in AD are still unknown.

Here, we provide an in-depth investigation of DA neurons in the VTA of Tg2576 mice with the aim of investigating features that might make these neurons particularly susceptible to degeneration. To address this objective, we focused on three different stages of the disease progression: before onset, at the onset and at an advanced state of neuronal degeneration. We show that, while in 1-month-old Tg2576 mice DA neurons behave normally, at the onset of neurodegeneration (3 months of age) these neurons undergo important changes in electrophysiological properties, accompanied by autophagic deficits. Dysfunctions in neuronal excitability further worsen in 6-month-old Tg2576 mice, an age-point characterized by pronounced DA cell death (Nobili et al., 2017), when we also observe significant changes in neuronal morphology. Interestingly, from 3 months of age, at the beginning of the neurodegenerative events, we also observed an enhanced c-Abl activation, restricted to the midbrain of Tg2576 mice. Accumulating evidence indicate that c-Abl is one of the factors involved in neurodegenerative diseases (Cancino et al., 2011; Imam et al., 2011; Jiang et al., 2005; Jing et al., 2009; Ko et al., 2010; Schlatterer et al., 2011; Tremblay et al., 2010) and its activation in AD and Parkinson's disease (PD) mouse models results in neurodegeneration by inhibition of the autophagic process. Thus, in an attempt to delay or block DA neuronal loss, we evaluated the efficacy of Nilotinib, a potent c-Abl inhibitor. Nilotinib has been effectively used to reverse the loss of DA neurons in PD models and to improve cognitive and motor performances *via* autophagic degradation of  $A\beta$  and  $\alpha$ -synuclein in models of AD and PD, respectively (Hebron et al., 2013a; Lonskaya et al., 2013b). Importantly, clinical trials showed that Nilotinib can reduce disease-related biomarkers in both AD and PD patients (Pagan et al., 2016, 2019; Turner et al., 2020). In accordance with these reports, here we show that an early and chronic *in vivo* administration of Nilotinib in Tg2576 mice mitigates disease progression by reducing  $A\beta$  load, blocking DA neuron degeneration and preventing morphological alterations in the VTA. The protection of DA neurons in the VTA of Tg2576 mice prevents the loss of DA outflow to the hippocampus and ameliorates cognitive functions.

Overall, the present data pinpoint the need of a deeper knowledge of the molecular bases of DA cell death and the identification of new pathways involved in the disease, to provide a framework for the design of new drugs and therapeutic strategies aimed at delaying or blocking the pathogenic events in AD.

## 2. Material and Methods

### 2.1. Animals and pharmacological treatment

Heterozygous Tg2576 mice (Hsiao et al., 1996) and WT littermates of either sex were used at 1, 3 and 6 months of age, as described in the text. All animal experiments were carried out in accordance with the ethical guidelines of the European Council Directive (2010/63/EU). Experimental approval was obtained from the Italian Ministry of Health (protocol #926/2018PR).

Nilotinib treatment started at 45 days of age. Animals were injected intraperitoneally (i.p.) with 1mg kg<sup>-1</sup> Nilotinib (Abcam; #ab142019) dissolved in 5% DMSO in saline, or with saline containing 5% DMSO alone (vehicle), on alternate days. All the experiments after treatment were performed at 3 and 6 months of age.

### 2.2. Brain slicing

Brain slicing was performed with as described in (Ting et al., 2018). All extracellular solutions were meant to better preserve neuronal morphology and function. The solutions were freshly prepared, then kept at 4°C for at most 5 days. All were saturated with a mixture of 95 %

O<sub>2</sub>, 5% CO<sub>2</sub> prior to usage; pH was checked daily to be between 7.3 and 7.4.

Acute brain slices were obtained following halothane anesthesia and transcardiac perfusion with a solution containing (in mM): 92 NMDG, 2.5 KCl, 1.2 NaH<sub>2</sub>PO<sub>4</sub>, 30 NaHCO<sub>3</sub>, 20 HEPES, 25 Glucose, 5 Na-Ascorbate, 2 Thiourea, 3 Na-Pyruvate, 10 MgSO<sub>4</sub>, 0.5 CaCl<sub>2</sub>. The brain was rapidly removed and horizontal slices (260 μm) containing the midbrain were cut with a vibratome (VT1200S, Leica) in chilled (4°C) perfusion solution. After cutting, brain slices were transferred to a holding chamber with 150 mL of the NMDG-based solution, and left to recover at 34°C. Recovery time was assigned to each animal based on its age and following Table 2 in (Ting et al., 2018), to gradually increase sodium concentration in order to preserve membrane integrity.

After the recovery procedure, slices were transferred to a long-term holding chamber containing the following solution (in mM): 92 NaCl, 2.5 KCl, 1.2 NaH<sub>2</sub>PO<sub>4</sub>, 30 NaHCO<sub>3</sub>, 20 HEPES, 25 Glucose, 5 Na-Ascorbate, 2 Thiourea, 3 Na-Pyruvate, 2 MgSO<sub>4</sub>, 2 CaCl<sub>2</sub>, where they were kept for the entire experimental session at room temperature.

### 2.3. Electrophysiological recordings

A single slice was placed into a recording chamber of an upright microscope (Axioskop 2-FS; Zeiss) and continuously perfused (3 mL sec<sup>-1</sup>, 32°C) with a solution containing (in mM): 124 NaCl, 2.5 KCl, 1.2 NaH<sub>2</sub>PO<sub>4</sub>, 24 NaHCO<sub>3</sub>, 5 HEPES, 12.5 Glucose, 2 MgSO<sub>4</sub>, 2 CaCl<sub>2</sub>.

The VTA was identified with infrared differential interference contrast (DIC) at a 4x magnification; neurons were visualized using a magnification of 60x.

Whole-cell patch-clamp and single-unit extracellular recordings were performed from DA neurons located in the VTA, subdivided in lateral and intermediate parts as in (Krashia et al., 2017; Zhang et al., 2010).

For whole-cell recordings, the target cell was approached with a glass capillary (TW-150F-4, World Precision Instruments, Germany) with a resistance of 3.5–4.5 MΩ and filled with a filtered solution containing (in mM): 120 K-Glu, 20 KCl, 0.2 EGTA, 10 HEPES, 2 MgCl<sub>2</sub>, 4 Mg-ATP, 0.3 Na-GTP, 10 Phosphocreatine, 0.2 % Biocytin, pH 7.30. After the formation of a giga-seal and membrane rupture, the following protocols were applied starting from a holding membrane potential of -60 mV:

- A voltage-clamp protocol consisting of a single -5 mV step (200 ms duration), for the evaluation of C<sub>m</sub>.
- A 1-minute long recording in I=0 to evaluate AP shape. The parameters were calculated with a custom-written MATLAB® script. The rise time and the decay time were calculated as the x-axis distance between the threshold potential and the peak potential, and between the peak potential and the minimum value reached during the hyperpolarization phase, respectively. The amplitude was calculated as the y-axis distance between the threshold and the peak. The width was defined as the duration between the threshold and the equipotential point found on the repolarization phase of the AP.
- A 1 s voltage-clamp protocol with 4 hyperpolarizing steps from -60 to -120 mV (Δ=20 mV), to study the amplitude of the I<sub>h</sub> current. The absolute I<sub>h</sub> current was calculated as the difference between the peak current value and the steady-state current reached during the -120 step, whereas the current density was obtained by dividing the absolute current to the respective C<sub>m</sub>.
- A voltage-clamp protocol consisting of a 100 ms depolarization from -60 to 0 mV to study the SK current, expressed as a peak right after the depolarizing current. Current density was obtained by dividing the absolute current value to C<sub>m</sub>.
- A voltage-clamp protocol made up of 4 hyperpolarizing steps lasting 500 ms from a holding potential of -25 mV, to study the inward KCNQ current relative to the steady state current.

For current-clamp recordings, cells were kept at -60 mV by direct

current injection. We applied a current-clamp protocol with steps of 50 pA lasting 600 ms, starting from -200 pA up to +200 pA, to evaluate the I/V relationship at sub-threshold potentials, the number of APs at above-threshold potentials, and the threshold and hyperpolarization potentials from the first action potential elicited by the +200 pA injection. Membrane resistance (R<sub>m</sub>) was calculated from the slope of the linear regression of I/V curves. The Sag amplitude was calculated as the difference between the lowest potential and the steady-state potential reached during the -200 pA hyperpolarizing step.

For post-synaptic spontaneous GABAergic currents (sIPSCs) the internal solution was switched to one containing (in mM): 130 CsCl, 1 EGTA, 10 HEPES, 2.5 QX-314-Cl, 2 Mg-ATP, 0.2 Na-GTP, 10 Phosphocreatine; pH 7.30. These currents were recorded in voltage-clamp at -70 mV, in the presence of (in μM): 10 NBQX-Na<sub>2</sub>, 50 AP-5, 1 CGP-55845, to block the activity of AMPA/Kainate, NMDA, and GABA<sub>B</sub> receptors, respectively.

Extracellular recordings were performed by filling the pipette with extracellular solution; the electrode was then moved towards a neuron's surface until firing was detected. Spikes were recorded on the I=0 mode, with high-pass (0.5 Hz) and low-pass filtering (1 kHz). DC components were also highpass-filtered by enabling 300 Hz AC coupling.

All signals were amplified with an Axon 700B amplifier, digitized at 20 kHz with a Digidata 1400A and computer-saved using Clampex 10.3 (all from Molecular Devices, Sunnyvale, CA).

During all experiments, the membrane access resistance was repeatedly monitored and recordings in which it exceeded over 25 % were discarded. No liquid junction potential correction was applied.

### 2.4. Adeno-associated virus (AAV) vector and stereotaxic injection

To monitor the autophagy flux, we utilized an adeno-associated virus (AAV2/9) carrying a monomeric tandem mCherry-GFP-LC3 (AAV2/9-mCherry-GFP-LC3) as a reporter construct (Castillo et al., 2013).

The virus was delivered via stereotaxic injection. Male mice were anaesthetized with Rompun (20 mg ml<sup>-1</sup>, 0.5 mL kg<sup>-1</sup>; Bayer) and Zoletil (100 mg ml<sup>-1</sup>, 0.5 mL kg<sup>-1</sup>; Virbac; i.p.) and positioned in a stereotaxic apparatus, before a burr hole was made under aseptic conditions. The viral vector (0.4 μL) was injected into the left VTA (-3.2 AP, ±0.35 ML, -4.4 DV; Paxinos and Franklin, 2012).

The virus (7.62 × 10<sup>13</sup> particles ml<sup>-1</sup>) was infused via 1 μL Hamilton syringe (Neuro7001; Hamilton; #65458-01) by slow pressure lasting 10 min using a Pump 11 Elite Nanomite Syringe Pump (Harvard Apparatus; flux 40 nl min<sup>-1</sup>) to allow for diffusion into the target brain area. Following infusion, the needle remained in place for at least an additional 8 min to prevent solution backflow, before being slowly retracted. After surgery the skin was sutured, and mice were returned to their home cage and monitored during recovery. Each animal was injected at postnatal day 70 (P70) and analyzed with immunofluorescence 21 days after surgery (P91). Data from animals showing misplaced injection site were discarded.

### 2.5. Immunohistochemistry and immunofluorescence

Mice were anaesthetized with Rompun (20 mg ml<sup>-1</sup>, 0.5 mL kg<sup>-1</sup>, i. p., Bayer) and Zoletil (100 mg ml<sup>-1</sup>, 0.5 mL kg<sup>-1</sup>, Virbac) and perfused transcardially with 50 mL saline followed by 50 mL of 4 % paraformaldehyde in Phosphate Buffer (PB; 0.1 M, pH 7.4).

The brains were removed and post-fixed in paraformaldehyde at 4°C and then immersed in 30 % sucrose solution at 4°C until sinking.

Brain sections for immunohistochemistry (TH/Nissl and c-Abl) were cut into 40 μm-thick coronal sections using a cryostat, and the slices were collected in PB. The sections (every second slice for a total of 9 sections) were incubated with primary antibody. The endogenous peroxidase was neutralized with a 0.3 % H<sub>2</sub>O<sub>2</sub> solution in PB. The sections were incubated overnight at 4°C with the primary antibody diluted in PB containing 0.3 % Triton X-100. After three washes in PB, sections

were incubated with a biotinylated secondary antibody followed by the avidin-biotin-peroxidase method (Vectastain, ABC kit, Vector) and using the chromogen 3,3'-diaminobenzidine (Sigma-Aldrich). Finally, sections were counterstained with Nissl staining, dehydrated and coverslipped with Entellan (Sigma-Aldrich). Immunohistochemistry brain sections were used for morphological analysis, c-Abl staining and cell counting (see below).

For TH/mCherry-GFP-LC3 immunofluorescent labelling, brains were cut into 30  $\mu\text{m}$ -thick coronal sections using a cryostat and the slices were collected in PB. The sections selected were processed with the primary anti-TH antibody in PB containing Triton 0.3 % over night. After three washes in PB, sections were incubated with a secondary antibody. For 3D reconstruction, images were taken as Z-stacks and these Z-stack images were then processed by maximum intensity projection. All samples were acquired with the same laser settings. For quantitative analysis, images were collected from at least 3–4 slices processed simultaneously from VTA and exported for analysis with ImageJ software.

For A $\beta$  quantification, slices were incubated for 2 nights with primary antibodies in PB containing Triton 0.3 % and then incubated for 2 h at room temperature with secondary antibodies. Quantification of A $\beta$  expression level in the different experimental groups was performed offline on confocal images by densitometric analyses. After background subtraction, the A $\beta$ -associated signal of neurons of specific brain regions was quantified by manually outlining individual neurons and measuring cell associated fluorescence intensity with the ImageJ software (<http://rsb.info.nih.gov/ij/>). The F/A ratio defines mean fluorescence of individual cells (F) normalized to total cellular surface (A). Quantification was done on 35 cells per region/mice (n=4 mice per group) and was conducted blind to the animal's experimental group.

For c-Abl visualization, slices were incubated for 2 nights with primary antibodies in PB containing Triton 0.3 % and then incubated for 2 h at room temperature with secondary antibodies.

Immunofluorescence analysis was also used for *post hoc* labeling of the recorded cells filled with biocytin (see "Electrophysiological recordings" section). Horizontal slices from electrophysiological recordings were fixed overnight in 4 % paraformaldehyde in PB, followed by 3 washes in PB and transferred to a 30 % sucrose solution at 4 °C until sinking. The slices were cut into 50  $\mu\text{m}$ -thick using a freezing microtome and collected in PB. The sections were incubated overnight at 4 °C with primary antibody and streptavidin red dye conjugate in PB containing 0.3 % Triton X-100. After three washes in PB, sections were incubated with a secondary antibody.

Primary antibodies: TH (1:1000, Millipore; MAB318; RRID: AB\_2201528); hAPP695 (6E10; 1:500, BioLegend; #803001; RRID: AB\_2564653); c-Abl (1:200, Santa Cruz; sc-56887; RRID: AB\_781732); NeuroTrace-405 (1:200, Thermo Fisher Scientific; #N21479).

Secondary antibodies: Alexa Fluor 488 donkey anti-mouse IgG (1:200; Thermo Fisher Scientific; #R37114; RRID: AB\_2556542), Alexa Fluor 405 goat anti-mouse IgG (1:200; Thermo Fisher Scientific; #A-31553; RRID: AB\_221604), biotinylated secondary antibody (Jackson ImmunoResearch Laboratories; #AP132B; RRID: AB\_11212148), streptavidin red dye (Alexa Fluor-546 conjugate, Thermo Fisher Scientific; #S11225; RRID: AB\_2532130).

Sections for immunofluorescence were coverslipped with Aqueous Mounting Media (Sigma-Aldrich) and examined under a confocal laser-scanning microscope (LSM700, Zeiss). The specificity of the immunofluorescence labelling was confirmed by the omission of primary antibodies and the use of normal serum instead (negative controls).

## 2.6. Morphological analysis

Sections processed for immunohistochemistry were used for morphological analysis of DA neurons. The VTA was divided into lateral and intermediate subregion, as described in the text. TH<sup>+</sup> cells were imaged with an optical microscope (DMLB; Leica) equipped with a

motorized stage and a camera connected to Neurolucida 7.5 software (MicroBright-Field) that allowed for quantitative 3D analysis of the entire cell body. For the measurement of neuronal cross-sectional area, Nissl staining was performed on TH stained sections. Only TH<sup>+</sup> neurons identified by a clear nuclear profile were included for analysis. Cell body area and perimeter were evaluated (Latini et al., 2014). Overall, twenty-five cells per lateral VTA and twenty-five cells per intermediate VTA per animal were selected randomly for analysis, and all data were subsequently averaged per subfield for each mouse.

## 2.7. Stereological analysis

Sections processed for immunohistochemistry were used for obtaining unbiased estimates of numbers of TH<sup>+</sup> neurons in the lateral VTA (the count refers to one hemisphere - see Fig. 3D) and for total number of TH<sup>+</sup> neurons in the entire VTA (Fig. 6B). The boundaries of the areas used for counting were defined by TH staining, and area distinction was performed according to Paxinos published guidelines (Paxinos and Franklin, 2012) and as described in the text. We applied an optical fractionator stereological design (bilateral count) using the Stereo Investigator System (MicroBrightField Europe e.K.). A stack of MAC 5000 controller modules (Ludl Electronic Products, Ltd) was interfaced with an Olympus BX50 microscope with a motorized stage and a HV-C20 Hitachi digital camera with a Pentium II PC workstation. A three-dimensional optical fractionator counting probe (x, y, z dimension of 50  $\times$  50  $\times$  25  $\mu\text{m}$ ) was applied. The brain area of interest was outlined using the 5x objective and neuronal cells were marked with a 100x oil-immersion objective. Neurons were considered TH<sup>+</sup> if they showed cytoplasmic TH immunoreactivity.

The total TH<sup>+</sup> neuron number was estimated according to the formula (Eq. 1):

$$N = SQ \times \frac{1}{ssf} \times \frac{1}{asf} \times \frac{1}{tsf} \quad (1)$$

where SQ represents the number of neurons counted in all optically sampled fields of the area of interest, ssf is the section sampling fraction, asf is the area sampling fraction and tsf is the thickness sampling fraction.

## 2.8. Transmission Electron Microscopy

Mice were anesthetized (as for immunohistochemistry studies) and perfused transcardially with a flush of saline solution followed by 4% freshly depolymerized paraformaldehyde and 0.2 % glutaraldehyde in 0.1 M phosphate buffer (PB; pH 7.4). Brains were removed, post-fixed in the same fixative for 30 days, cut on a Vibratome in 50  $\mu\text{m}$  serial horizontal sections from the midbrain and collected in PB until processing (Melone et al., 2019). Horizontal sections were obtained through the dorso-ventral extent of the VTA, resulting in 12–13 sections per series. To verify the dorso-ventral extension of VTA, the first and the last section from all series were processed for immunoperoxidase detection of TH using an anti-TH primary antibody (1:400; Millipore, #AB1542; RRID:AB\_90755; Murphy and Deutch, 2018), followed by the embedding procedure as previously described (Melone et al., 2019).

### 2.8.1. Post-embedding procedure

Sections were processed for an osmium-free embedding method (Melone et al., 2019; Phend et al., 1995). Dehydrated sections were immersed in propylene oxide, infiltrated with a mixture of Epon/Spurr resins, sandwiched between Aclar films, and polymerized at 60 °C for 48 h. After polymerization, chips from the intermediate VTA (Krashia et al., 2017; Morales and Margolis, 2017) were cut from the wafers, glued to blank resin blocks and sectioned with an ultramicrotome. Thin sections (60–80 nm) were cut and mounted on 300 mesh nickel grids and processed for immunogold labeling (Melone et al., 2019; Phend et al.,

1995). In brief, after treatment with 4 % para-phenylenediamine in Tris-buffered saline (0.1 M Tris, pH 7.6, with 0.005 % Tergitol NP-10; TBST), grids were washed in TBST (pH 7.6), transferred for 15 min in 0.25 % NDS in TBST (pH 7.6) and then incubated overnight (28°C) in a solution of TBST (pH 7.6) containing anti-TH primary antibody (1:200; Abcam; #AB1542; RRID:AB\_90755). Grids were subsequently washed in TBST (pH 8.2), transferred for 10 min in 0.5 % NDS in TBST (pH 8.2), incubated for 2 h (28°C) in TBST (pH 8.2) containing secondary antibodies conjugated to 18 nm gold particles (1:20; Jackson, 713–215-147; RRID: AB\_2340734), washed in distilled water, and then stained with uranyl acetate and Sato's lead. The optimal concentration of antibodies was sought by testing several dilutions; the concentration yielding the lowest level of background labeling and still immunopositive elements was used to perform the final studies. Gold particles were not detected when primary antiserum was omitted. When normal serum was substituted for immune serum, sparse and scattered gold particles were observed, but they did not show any specific relationship to subcellular compartments. Ultrathin sections were examined with a Philips CM10 electron microscope coupled to a MegaView-II high resolution CCD camera (Soft Imaging System). Identification of ultrastructural profiles was based on established morphological criteria (Peters et al., 1991).

### 2.8.2. Data collection and analysis

Immunogold labeled cytoplasm of neurons were randomly acquired from 12 ultrathin sections/animal. For determining the density of gold particles of labeled fields, particles were counted and areas were calculated using ImageJ software. Background was calculated by estimating labeling density over neuronal nuclei (Melone et al., 2019). In each cytoplasmic fields, double-membraned autophagosomes were identified according to well established criteria (Eskelinen, 2008; Kliensky et al., 2021; Ylä-Anttila et al., 2009), and their density calculated.

### 2.9. Total protein extraction

The midbrain was dissected from the entire brain. Tissue was homogenized in RIPA buffer containing (in mM): 50 Tris-HCl pH 7.5, 150 NaCl, 5 MgCl<sub>2</sub>, 1 EDTA, 1% Triton X-100, 0.25 % sodium deoxycholate, 0.1 % SDS, 1 sodium orthovanadate, 5 b-glycerophosphate, 5 NaF and protease inhibitor cocktail, and incubated on ice for 30 min (Nobili et al., 2018). The samples were centrifuged at 15,000g for 20 min and the protein concentration of the supernatant was determined by the Bradford method.

### 2.10. Immunoblotting analysis

Proteins were applied to SDS-PAGE and electroblotted on a polyvinylidene difluoride (PVDF) membrane. Immunoblotting analysis was performed using a chemiluminescence detection kit. The relative levels of immunoreactivity were determined by densitometry using the ImageJ software.

Primary antibodies: p-c-Abl Tyr 412 (1:500; Santa Cruz, #sc-293130; RRID: AB\_2220986); c-Abl (1:500; Santa Cruz; #sc-56887; RRID:AB\_781732); GAPDH (1:50000; Calbiochem; #CB1001; RRID: AB\_2107426); LC3 (1:500; Cell Signaling; #4108; RRID: AB\_2137703).

Secondary antibodies: goat anti-mouse IgG (1:3,000; Bio-Rad; #1706516; RRID: AB\_11125547), goat anti-rabbit IgG (1:3,000; Bio-Rad; #1706515; RRID: AB\_2617112).

Membranes were stripped using Re-Blot Plus Strong Solution (Millipore) for 15 min at room temperature.

### 2.11. Microdialysis

Male mice, anaesthetized with Rompun (20 mg ml<sup>-1</sup>, 0.5 mL kg<sup>-1</sup>, i. p., Bayer) and Zoletil (100 mg ml<sup>-1</sup>, 0.5 mL kg<sup>-1</sup>, Virbac), were mounted on a stereotaxic frame and implanted unilaterally with

microdialysis probes 24–36 h before experiments. The concentric dialysis probes (AN69 fibres, Hospal Dasco) were implanted vertically at the level of the hippocampus (AP -3.0, ML ±2.7 from bregma). The probe lengths were 5 mm (3 mm membrane).

Each probe was fixed and the skin was sutured. Mice were returned to their home cages and the outlet and inlet probe tubing were protected by locally applied parafilm. Membranes were tested for *in vitro* recovery before surgery. On the day of the experiment each animal was placed in a circular cage containing microdialysis equipment: the microdialysis probe was connected to a CMA/100 pump (Carnegie Medicine) through PE-20 tubing and an ultralow torque multichannel power-assisted swivel (Model MCS5, Instech Laboratories) to allow free movement. Artificial cerebrospinal fluid (in mM: NaCl 140; KCl 4; CaCl<sub>2</sub> 1.2; MgCl<sub>2</sub> 1) was pumped through the dialysis probe (2.1 μL min<sup>-1</sup>). Following the start of the dialysis perfusion, mice were left undisturbed for ~1 h before the collection of six baseline samples. Dialysate samples were collected every 20 min for 120 min. Brains were then post-fixed in 4% paraformaldehyde, cut in coronal slices (100 μm) and processed for methylene blue staining. The correct positioning of the probes was confirmed under a microscope. Data from animals not showing proper placement were discarded.

Each dialysate sample (20 μL) was analyzed by ultra-performance liquid chromatography. Concentrations (pg 20 μL<sup>-1</sup>) were not corrected for probe recovery. The ultra-performance liquid chromatography apparatus (ACQUITY, Waters Corporation) was coupled to an amperometric detector (Decade II, Antec Leyden) containing an *in-situ* Ag/AgCl reference electrode and an electrochemical flow-cell (VT-03, Antec Leyden) with a 0.7 mm glassy carbon electrode, mounted with a 25 mm spacer. The electrochemical flow-cell, set at a potential of 400 mV, was positioned immediately after a BEH C18 column (2.1 × 50 mm, 1.7 μm particle size; Waters Corporation). The column was kept at 37°C (0.07 mL min<sup>-1</sup> flow rate). The composition of the mobile phase was (in mM): 50 phosphoric acid, 8 KCl, 0.1 EDTA, 2.5 1-octanesulfonic acid sodium salt, 12 % MeOH and pH 6.0 adjusted with NaOH. Peak height obtained by oxidation of DA was compared with that produced by a standard. The detection limit was 0.1 pg.

### 2.12. Novel Object Recognition Test (NORT)

The NORT is a validated test to measure recognition memory in rodents by exploiting their natural tendency to explore novel items (Cohen and Stackman, 2015), and it is strictly dependent on hippocampal integrity (Jessberger et al., 2009; Squire et al., 2007).

Mice were tested individually in a Plexiglass arena (56 × 42 × 21 cm) not directly illuminated. The NORT encompasses three main sessions: habituation, training, and tests (Bardgett et al., 2011; Cutuli et al., 2014; Gerenu et al., 2013).

In the habituation session, mice were familiarized with the empty arena for 5 min. In the training session (after a 3-min delay spent in their home cages following habituation), mice were allowed to explore two identical objects (*i.e.*, white plastic spheres), placed in the middle of the arena, equidistant from the center, for 5 min. After 1 h and 24 h, the test sessions were performed by replacing one of the two identical objects with an unfamiliar novel object (*i.e.*, a light grey wooded cone or a black plastic spool, respectively) and observing animals' exploration of the objects (*i.e.*, when they touched them with the snout or sniffed them) for 5 min. Objects and arena were cleaned with 30 % ethanol between sessions to minimize olfactory signals.

The NORT parameters considered were the contact time (s) with objects during training and test sessions and the number of defecation boluses during each session of the task.

### 2.13. Sample size, randomization and blinding

The number of samples in each group and for each experiment was determined based on published studies. All randomization was

performed by assigning a random number to each animal and using a random number table. All data were collected by researchers that were blind to the genotype or pharmacological treatment of each animal.

#### 2.14. Statistical analysis

All statistical analysis was performed with GraphPad Prism (v7.00), except for the three-way analysis of variances (ANOVA), which was performed with MATLAB® (R2019b, Mathworks, Inc.).

TH<sup>+</sup> stereological cell count and cell morphology in naïve animals were analyzed by Two-Way ANOVA with genotype (WT vs Tg) and VTA subregions (lateral vs intermediate) as independent factors.

Following Nilotinib treatment, cell count and cell morphology were analyzed by two-way ANOVA for genotype (WT vs Tg) and treatment (Veh versus Nil). Microdialysis data were analyzed by ordinary two-way ANOVA for time vs treatment.

Two-way repeated measures ANOVA was used to analyze neuron excitability data (number of action potentials, with genotype as an independent factor, and drive current as a repeated factor) and the M Current (with genotype as an independent factor, and membrane potential as a repeated factor).

The change in weight the animals endured during the pharmacological treatment was analyzed with a three-way ANOVA; accordingly, the factors were treatment (Veh vs Nil), genotype (WT vs Tg), and weight (once per week).

All post hoc comparisons following ANOVAs were assessed with Tukey's or Sidak's tests.

The rest of the data were checked for normality by using the D'Agostino and Pearson or Shapiro-Wilk normality tests and analyzed accordingly with two-tailed parametric (Student's *t*-test, Welch's *t*-test, Paired *t*-test) or non-parametric tests (Mann-Whitney, Kolmogorov-Smirnov or Kruskal-Wallis tests).

See figure legends for more details. Values of  $p \leq 0.05$  were considered to be statistically significant.

In the box-and-whisker plots, the center line denotes the median value, edges are upper and lower quartiles, whiskers show minimum and maximum values and points are individual experiments.

All other data are presented as mean  $\pm$  s.e.m.

### 3. Results

#### 3.1. Increased excitability of DA neurons in the VTA of Tg2576 mice

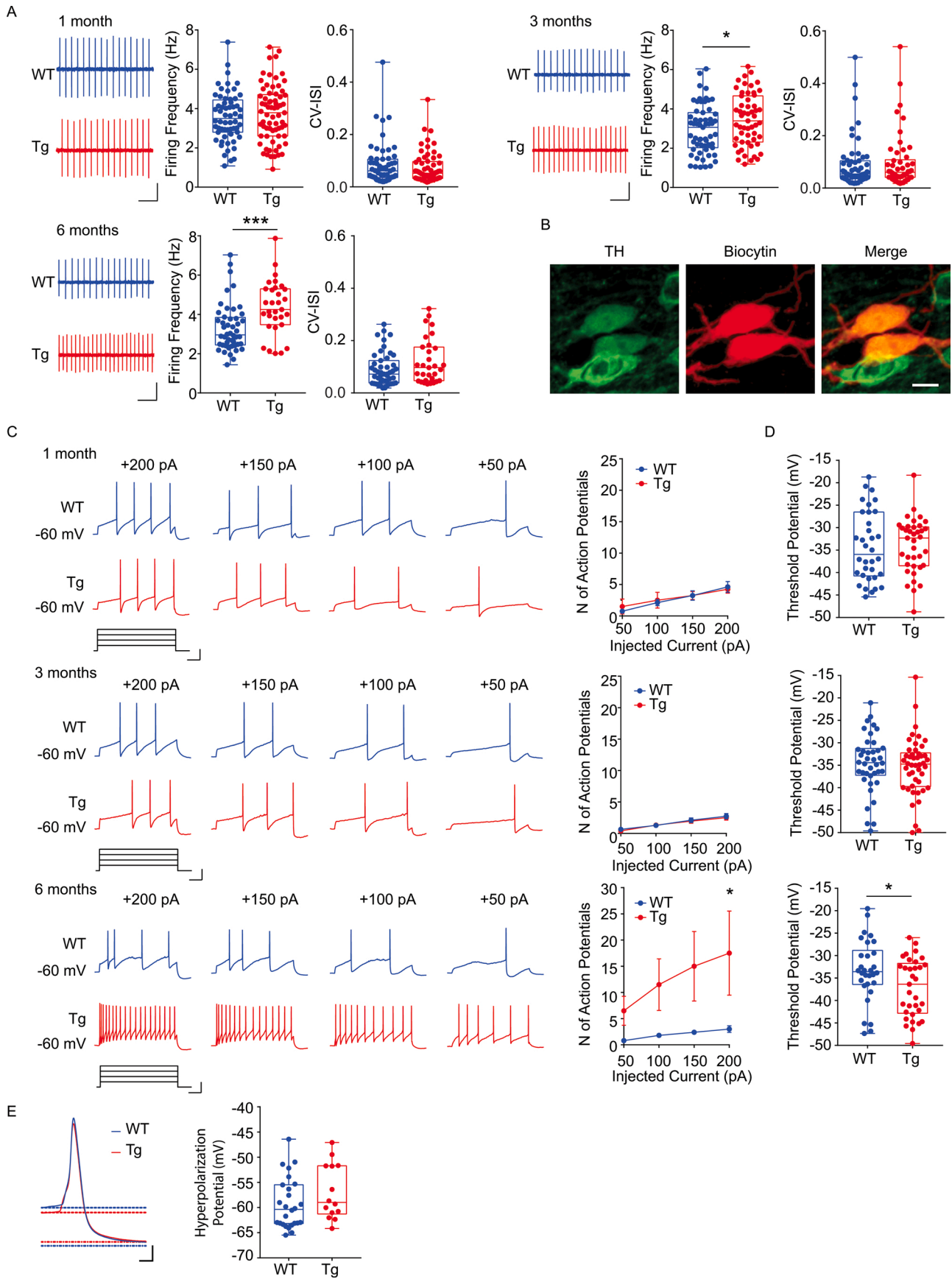
Degeneration of VTA DA neurons in the Tg2576 mouse model of AD is detectable since the age of 3 months, and it worsens over time. Loss of tyrosine hydroxylase positive (TH<sup>+</sup>) terminals in the dorsal hippocampus and NAc shell results in a prominent drop of DA outflow to these projection areas and in a deficit of synaptic plasticity, followed by impairments in memory and reward performance in 6-month-old Tg2576 mice (Cordella et al., 2018; Nobili et al., 2017). As a functional readout of neuronal status, we performed electrophysiological recordings from DA neurons in the VTA of 1-, 3- and 6-month-old Tg2576 and age-matched wild-type (WT) mice to study the functional properties of these cells before the onset, at the onset and at an advanced phase of neuronal degeneration, respectively.

Since DA cells in the VTA are spontaneously active, we first performed extracellular single-unit recordings from midbrain slices to compare spontaneous action potential (AP) firing frequency and pacemaker regularity between the two genotypes. While at 1 month of age no differences could be seen between WT and Tg2576 neurons, DA neurons from 3-month-old Tg2576 mice displayed an increased spontaneous firing frequency, that became even more prominent at 6 months of age (Fig. 1A). These data suggest that firing alterations in DA neurons of Tg2576 mice are just beginning at 3 months of age and worsen with age. Firing regularity, as measured by the coefficient of variation of the interspike interval (CV-ISI), was unchanged at all ages (Fig. 1A).

To further investigate the excitability of Tg2576 DA neurons, we studied the active and passive properties of identified neurons by combining patch-clamp techniques with confocal TH-labelling of biocytin-filled neurons (Fig. 1B). Given the high degree of variability in the firing properties of VTA neurons along the medio-lateral axis (Krashia et al., 2017; Morales and Margolis, 2017; Roeper, 2013; Zhang et al., 2010), we analysed separately the results from lateral vs intermediate neurons. Overall, irrespective of genotype or age, intermediate VTA neurons showed a higher propensity to fire APs in response to depolarizing currents compared to lateral VTA DA neurons (compare Fig. 1C with Supplementary Fig. 1A). In 1- and 3-month-old Tg2576 mice the ability of DA neurons to fire APs was unchanged compared to WT neurons, yet the firing rate was particularly enhanced in 6-month-old Tg2576 mice (Fig. 1C; Supplementary Fig. 1A). These results suggest an increased excitability of DA neurons in 6-month-old Tg2576 mice, and an increased functional output both during spontaneous pacemaking and in response to current input. The increased excitability of 6-month-old Tg2576 DA neurons, pooled together from both VTA subregions, was not due to differences in cell capacitance or membrane resistance (Supplementary Table 1, see also Supplementary Fig. 1B). On the other hand, it was strongly correlated with a significant shift of the AP threshold to more negative values in 6-month-old Tg2576 neurons (Fig. 1D,E), while we also observed a faster deactivation of the AP (Supplementary Table 1). Additionally, though not significant, the after-hyperpolarization potential reached during pacemaking was less negative in Tg2576 neurons compared to WT cells (Fig. 1E), suggesting a reduction in the after-hyperpolarization current. Indeed, depolarization to 0 mV induced a smaller after-hyperpolarization current in 6-month-old Tg2576 mice (Fig. 2A), known to be mediated mainly by Small-Conductance Calcium-Activated K<sup>+</sup> (SK) channels (Krashia et al., 2019a). Even though the reduction in the SK-mediated conductance would be compatible with the increased excitability of DA neurons in 6-month-old Tg2576 mice, the difference between genotypes was too small. Indeed, when the SK current was plotted as the current density relative to cell size, we found no difference compared to WT neurons at 3 or 6 months of age (Fig. 2A) and only a small reduction in neurons of younger Tg2576 animals (Supplementary Fig. 2A).

Next, we examined other characteristic DA neuron conductances, namely the hyperpolarization-activated current (I<sub>h</sub>) mediated by HCN channels (Mercuri et al., 1995; Neuhoff et al., 2002; Seutin et al., 2001) and the non-inactivating M-Current mediated by the KCNQ channel family (Koyama and Appel, 2006). The I<sub>h</sub> is an inward K<sup>+</sup>/Na<sup>+</sup> current while KCNQ channels are voltage-gated K<sup>+</sup> channels. Together with SK channels, these conductances play an essential role in regulating action potential repolarization, synaptic plasticity and synchronous activity in neurons (Engel and Seutin, 2015; Gasselin et al., 2015; He et al., 2014; Huang et al., 2011; Koyama and Appel, 2006; Masi et al., 2015). We did not observe any difference between genotypes in the magnitude of the I<sub>h</sub> current at 1 and 3 months of age (Supplementary Fig. 2B), while in 6-month-old Tg2576 DA cells the I<sub>h</sub> current was reduced compared to WT neurons (Fig. 2B). In line with the reduction in I<sub>h</sub>, the voltage 'sag' observed during cell hyperpolarization was also reduced in 6-month-old Tg2576 mice (Supplementary Fig. 1B). However, similarly to SK currents, a closer look at the I<sub>h</sub> current density relative to cell size indicated no difference compared to WT neurons (Fig. 2B). Additionally, the M-Current (I<sub>m</sub>), measured with voltage steps from -35 mV to -65 mV showed no differences between genotypes for any of the three age groups (Fig. 2C and Supplementary Fig. 2C).

Overall, the subtle alterations in I<sub>h</sub>- and SK-mediated conductances and the early changes in the spontaneous and evoked excitability of Tg2576 DA neurons are all indications of cellular dysfunction. Given that the majority of afferents onto DA neurons of the VTA – as much as 70 % of synaptic inputs – are GABAergic and have a major impact on the activity of DA cells (Henny et al., 2012; Mathon et al., 2003; White, 1996; Yang et al., 2018), we next examined whether alterations in the GABAergic input on Tg2576 DA neurons could contribute to the



(caption on next page)

**Fig. 1.** Increased firing of DA neurons in the VTA from Tg2576 mice.

**A.** Spontaneous firing recorded from DA neurons of the VTA (scale: 1 s; 2 mV) in 1-, 3- and 6-month-old WT and Tg2576 (Tg) mice and respective plots showing instantaneous firing frequency and the coefficient of variation of the interspike interval (1 month: WT: n = 60 neurons, 5 mice; Tg: n = 69 neurons, 5 mice; Unpaired *t*-test for frequency, *p* = 0.465; Mann-Whitney test for CV-ISI, *p* = 0.830; 3 months: WT: n = 59 neurons, 11 mice; Tg: n = 55 neurons, 10 mice; Unpaired *t*-test for frequency, \**p* = 0.044; Mann-Whitney test for CV-ISI, *p* = 0.871; 6 months: WT: n = 48 neurons, 9 mice; Tg: n = 31 neurons, 7 mice. Mann-Whitney test for frequency, \*\*\**p* = 0.0007; Kolmogorov-Smirnov test for CV-ISI, *p* = 0.538).

**B.** Confocal images (scale: 10 μm) showing TH-positive labelling (in green) of two recorded, biocytin-filled neurons (in red).

**C.** APs recorded in current-clamp following 50 pA-stepped positive current injections (scale: 100 ms; 20 mV; 100 pA) in lateral DA neurons held at -60 mV and plots demonstrating the average number of action potentials (± s.e.m.) elicited at each depolarizing step (1 month: WT: n = 8 neurons, 4 mice; Tg: n = 5 neurons, 3 mice; Two-Way repeated-measures ANOVA for Genotype vs Depolarization: Interaction:  $F_{4,44} = 0.4136$ , *p* = 0.798; Genotype:  $F_{1,11} = 0.016$ , *p* = 0.856; Depolarization:  $F_{4,44} = 27.41$ , *p* < 0.0001; 50 pA: *p* = 0.953; 100 pA: *p* = 0.998; 150 pA: *p* > 0.999; 200 pA, *p* = 0.998 with Sidak post-hoc test; 3 months: WT: n = 22 neurons, 7 mice; Tg: n = 22 neurons, 9 mice; Two-Way repeated-measures ANOVA: Interaction:  $F_{4,168} = 0.248$ , *p* = 0.911; Genotype:  $F_{1,42} = 0.105$ , *p* = 0.748; Depolarization:  $F_{4,168} = 69.79$ , *p* < 0.0001; 50 pA: *p* = 0.986; 100 pA: *p* > 0.999; 150 pA: *p* = 0.999; 200 pA, *p* = 0.986 with Sidak post-hoc test; 6 months: WT: n = 7 neurons, 6 mice; Tg: n = 11 neurons, 5 mice; Two-Way repeated-measures ANOVA: Interaction:  $F_{4,64} = 3.39$ , *p* = 0.014; Genotype:  $F_{1,16} = 4.498$ , *p* = 0.049; Depolarization:  $F_{4,64} = 7.189$ , *p* < 0.0001; 50 pA: *p* = 0.820; 100 pA: *p* = 0.170; 150 pA: *p* = 0.064; 200 pA, \**p* = 0.023 with Sidak post-hoc test).

**D.** Threshold potential measured from the first AP elicited by a +200 pA depolarizing step (1 month: WT: n = 34 neurons, 5 mice; Tg: n = 37 neurons, 5 mice; Unpaired *t*-test, *p* = 0.857; 3 months: WT: n = 40 neurons, 7 mice; Tg: n = 46 neurons, 9 mice; Unpaired *t*-test, *p* = 0.628; 6 months: WT: n = 30 neurons, 9 mice; Tg: n = 33 neurons, 7 mice; Unpaired *t*-test, \**p* = 0.032).

**E.** The traces show representative APs from a WT and a Tg DA neuron at 6 months of age (scale: 2 ms; 10 mV). Dashed lines show the threshold potential and the after-hyperpolarization potential. The graph shows the lowest point reached during the repolarizing phase in 6-month old mice (WT: n = 26 neurons, 7 mice; Tg: n = 14 neurons, 7 mice; Mann-Whitney test, *p* = 0.162).

In this and all other Figures, in box-and-whisker plots the centre line shows the median value, edges are upper and lower quartiles, whiskers show minimum and maximum values, and each point is an individual experiment.

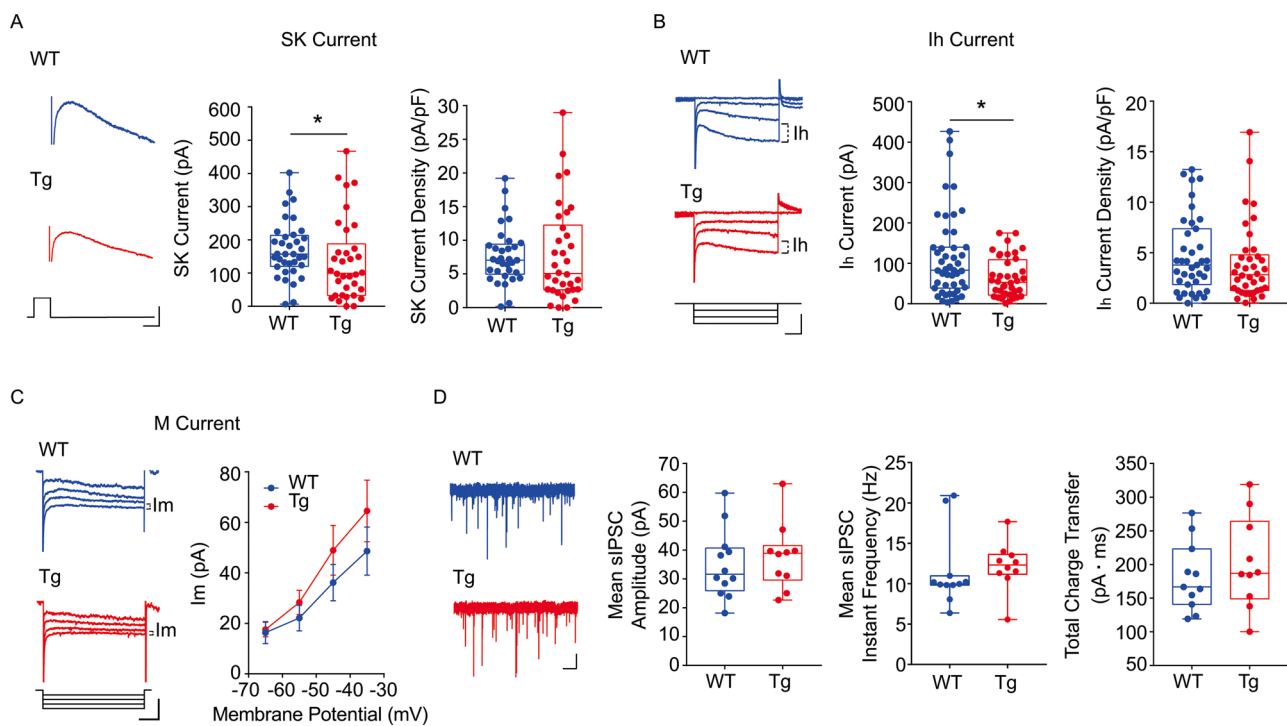


**Fig. 2.** Characteristic conductances and GABAergic input of VTA DA neurons in Tg2576 mice.

**A.** Traces show SK-mediated currents measured after depolarization from -60 to 0 mV (traces scale: 20 ms; 50 mV, protocol scale: 100 ms; 60 mV). The plots show peak SK current amplitude (WT: n = 36 neurons, 8 mice; Tg: n = 34 neurons, 9 mice; Kolmogorov-Smirnov test, \**p* = 0.020) and SK current density (WT: n = 33 neurons, 8 mice; Tg: n = 34 neurons, 9 mice; Welch's *t*-test, *p* = 0.888) at 6 months of age.

**B.** *I<sub>h</sub>* current traces obtained with -20 mV-stepped hyperpolarizations from -60 mV to -120 mV (scale: 100 ms; 100 pA; 60 mV). The plots show *I<sub>h</sub>* current amplitude at -120 mV (WT: n = 47 neurons, 8 mice; Tg: n = 40 neurons, 9 mice; Kolmogorov-Smirnov test, \**p* = 0.026) and *I<sub>h</sub>* density (WT: n = 39 neurons, 8 mice; Tg: n = 38 neurons, 9 mice; Kolmogorov-Smirnov test, *p* = 0.629) at 6 months of age.

**C.** M-current traces (scale: 100 ms; 100 pA; 40 mV) recorded after four 10 mV-hyperpolarizing steps from a holding potential of -25 mV. The plot show mean current amplitude (± s.e.m.) at the different membrane potentials (WT: n = 15 neurons, 4 mice; Tg: n = 21 neurons, 5 mice; Two-Way repeated-measures ANOVA: Interaction:  $F_{3,99} = 0.941$ , *p* = 0.424; Genotype:  $F_{1,33} = 0.806$ , *p* = 0.376; Potential:  $F_{3,99} = 27.2$ , *p* < 0.0001; -35 mV - -65 mV: *p* > 0.05 with Sidak post-hoc test) in 6-month old mice.

**D.** Sample traces of sIPSCs recorded from 3-month-old DA neurons (held at -70 mV) in WT and Tg mice (scale: 500 ms; 20 pA). The plots show amplitude, instantaneous frequency, and total charge transfer of sIPSCs (Amplitude: WT: n = 12 neurons, 4 mice; Tg: n = 10 neurons, 5 mice; Unpaired *t*-test: *p* = 0.577; Frequency: WT: n = 12 neurons, 4 mice; Tg: n = 10 neurons, 5 mice; Mann-Whitney test for Frequency: *p* = 0.059; Total Charge Transfer: WT: n = 11 neurons, 4 mice; Tg: n = 10 neurons, 5 mice; Unpaired *t*-test, *p* = 0.439).

increased spontaneous firing activity we observed at 3 months of age (see Fig. 1A). However, analysis of spontaneous inhibitory post-synaptic currents (sIPSCs) recorded from WT and Tg2576 neurons showed no difference across genotypes for either current amplitude, event frequency, or total charge transfer (Fig. 2D), overall suggesting that changes in the inhibitory input do not appear to be responsible for the increased firing frequency of Tg2576 DA neurons.

### 3.2. DA cell soma alterations in the VTA of 6-month-old Tg2576 mice

We next sought to determine how the progressive DA neuron degeneration occurring in the VTA of Tg2576 mice (Nobili et al., 2017) could be correlated with morphology alterations. To this aim, we investigated the soma area and perimeter of DA neurons in the VTA of mice at 3 and 6 months of age. DA neurons are not only functionally heterogeneous, but also show differences in size along the medio-lateral axis, such that the smallest neurons are located within the intermediate region, and the largest neurons in the lateral part (Krashia et al., 2017). For this reason, we subdivided the VTA into intermediate and lateral parts for a more detailed analysis of soma parameters (Fig. 3A).

We confirmed that at 3 and 6 months of age the soma size of WT DA neurons differs depending on the location along the medio-lateral axis. By comparing the two genotypes, we saw that at 3 months of age there were no differences between WT and Tg2576 neurons in soma area or perimeter in both the lateral and intermediate VTA (Fig. 3B). Even though no differences were noticed in the intermediate subregion compared to WT neurons at 6 months of age, we observed a strong reduction of both area and perimeter in Tg2576 cells in the lateral part of the VTA (Fig. 3C). These data could suggest that lateral neurons in 6-month-old Tg2576 mice undergo shrinkage and/or that larger neurons degenerate so that the surviving neurons we studied are smaller. We therefore used stereology to quantify the survival of DA neurons at 3- and 6-months of age, this time by focusing only on the lateral subfield of the VTA rather than on the entire area (Nobili et al., 2017). As shown in Fig. 3D, we observed a strong tendency for reduction in the number of lateral DA neurons at 6 months of age that was, however, not significant but might suggest that the reduction in cell size/perimeter of lateral VTA neurons in 6-month-old Tg2576 mice could be correlated with degeneration.

### 3.3. Autophagy alterations in DA neurons in the VTA of Tg2576 mice

DA neurons have physiological characteristics that make them particularly vulnerable (Chan et al., 2010), such as long axons, poorly or completely unmyelinated, that provide massive projections in the target areas (Braak et al., 2006). In addition, these cells have an autonomous pacemaker activity which could contribute to their vulnerability due to the high metabolic demand and need of efficient mitochondrial function. Therefore, efficient axonal transport and autophagy mechanisms are needed for the removal of damaged mitochondria and the regeneration of synaptic components. In support of the importance of the autophagic process in DA neurons, autophagy impairment has been strongly linked to the degeneration of SNpc DA neurons in PD (Hunn et al., 2019; Isidoro et al., 2009; Sato et al., 2018), yet any link between autophagy deficits and degeneration of VTA neurons in AD is still missing. To this aim, we used transmission electron microscopy (TEM) in 3-month-old mice to investigate potential alterations in autophagy processes in Tg2576 mice (Fig. 4A). In TH post-embedded material from WT and Tg2576 animals, DA neurons were identified based on the density of cytoplasmic TH-coding particles (Fig. 4A,B). In the cytoplasm of both WT and Tg2576 neurons we detected double-membraned autophagosomes (Fig. 4A) characterized by electron dense material at different stages of degradation (Klionsky et al., 2021). In line with our hypothesis, VTA DA neurons from Tg2576 mice showed an increased density of autophagosomes in their cytoplasm compared to cells from WT mice (Fig. 4C).

Therefore, in order to analyse the autophagy flux in TH<sup>+</sup> neurons from 3-month-old Tg2576 mice, we inoculated the VTA of mice with an adeno-associated virus (AAV) carrying the dynamic fluorescent reporter mCherry-GFP-LC3 (AAV2/9- mCherry-GFP-LC3; Castillo et al., 2013). LC3 is a cytosolic protein that plays a crucial role in the formation of autophagosomes (Tanida et al., 2005). The GFP fluorescence produced by this AAV is sensitive to the acidic and/or proteolytic conditions of the lysosome lumen, while mCherry retains its fluorescence even at acidic pH (Matus et al., 2014). Therefore, the co-localization of both mCherry and GFP fluorescence (visualized as yellow puncta) stains a vesicular compartment that has not yet fused with lysosomes (phagophores or autophagosomes), whereas an mCherry vesicle (red puncta) corresponds to an autophagolysosome. In the TH<sup>+</sup> neurons of Tg2576 mice we observed an increase in total puncta, suggesting an increase in LC3 in all the compartments of the autophagy-lysosomal pathway (Fig. 4D), confirming our TEM results (see Fig. 4C). Quantification of yellow puncta in VTA TH<sup>+</sup> cells showed a significant increase in Tg2576, indicating an increase in autophagosome numbers, while the number of autophagolysosomes (red puncta) was invariant. Moreover, the analysis of the dynamics of LC3 vesicles (mCherry/yellow ratio) suggests that the autophagosome clearance is impaired in DA neurons from 3-month-old Tg2576 mice. These alterations were also confirmed by western blotting analysis showing an increase of the LC3II/LC3I ratio in the midbrain of Tg2576 mice (Fig. 4E).

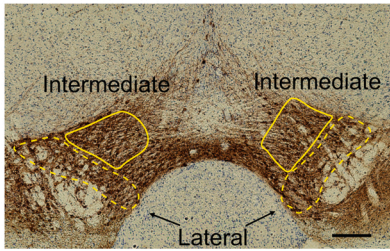
Given that numerous proteins regulate the autophagic process, we next focused on the expression levels of c-Abl, with the aim of examining further the basis for autophagy dysfunctions in Tg2576 neurons. c-Abl is a tyrosine kinase whose increased activity can lead to failure of autophagic protein clearance through the lysosome, resulting in the accumulation of toxic substrates (Abushouk et al., 2018; Lonskaya et al., 2014). Indeed, emerging evidence shows that alterations in c-Abl activity play a central role in several neurodegenerative diseases, including PD and AD (Gonfloni et al., 2012; Hebron et al., 2013a; Imam et al., 2011; Jing et al., 2009; Karuppagounder et al., 2014; Ko et al., 2010; Lindholm et al., 2016; Schlatterer et al., 2011). By using light and confocal microscopy we first confirmed that c-Abl is highly expressed in VTA DA neurons (Supplementary Fig. 3A,B). Next, we evaluated c-Abl activity by measuring the levels of its phosphorylated form in the midbrain of 3-month-old WT and Tg2576 animals. Particularly, we examined the phosphorylation of tyrosine residue 412 (p-c-Abl Y412) that has been shown to be important for c-Abl activation and colocalization with degenerating hippocampal neurons in AD subjects (Jing et al., 2009). Although the basal (total) midbrain levels of c-Abl were unchanged between WT and Tg2576, we observed an increased phosphorylation of c-Abl in Tg2576 mice (Fig. 4E). Interestingly, the increased phosphorylation appears to be restricted to the midbrain, since no changes in c-Abl phosphorylation was observed in other brain regions such as the hippocampus, amygdala, and cortex (Supplementary Fig. 3C-E). Furthermore, we did not observe any changes in LC3II/LC3I ratio in these regions (Supplementary Fig. 3), indicating no alterations in the autophagic process, at least at this age.

These data prove an increased activity of the c-Abl tyrosine kinase in the midbrain of 3-month-old Tg2576 mice, that might contribute to the autophagy alterations observed in DA neurons.

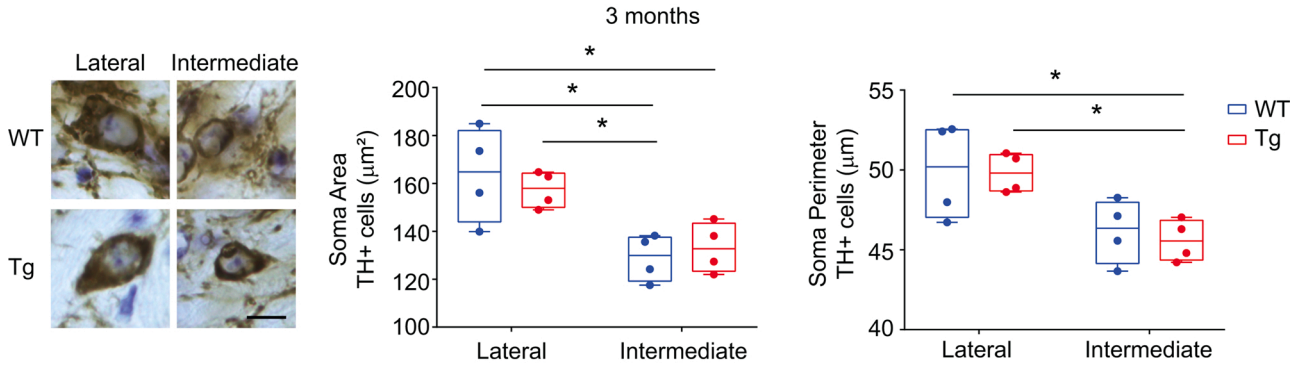
### 3.4. Nilotinib improves autophagy flux and reduces A $\beta$ load in 3-month-old Tg2576 mice

Since c-Abl has been identified as an important pathogenic mediator of neurodegenerative diseases (Alvarez et al., 2004; Imam et al., 2011; Jing et al., 2009; Ko et al., 2010; Schlatterer et al., 2011), many studies have successfully investigated the therapeutic potential of c-Abl inhibitors (Cancino et al., 2011, 2008). One of these – Nilotinib (commercial name Tasigna) – a potent c-Abl inhibitor approved by the U.S. FDA for adults with chronic myeloid leukemia, has been shown to reverse the loss of DA neurons in PD models and to improve

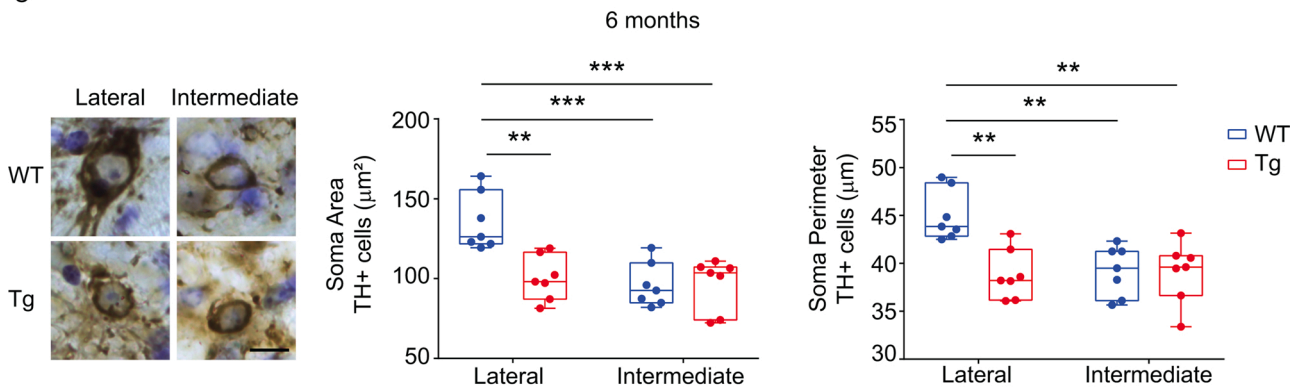
A



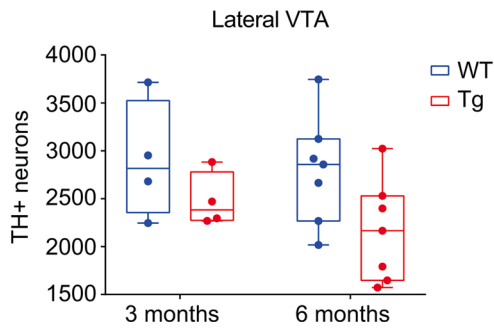
B



C



D



(caption on next page)

**Fig. 3.** DA neuron soma alterations in the VTA of 6-month-old Tg2576 mice.

**A.** Coronal midbrain section showing the lateral and intermediate VTA subregions used for the morphological and stereological analysis of TH<sup>+</sup> neurons (scale: 500  $\mu$ m).

**B.** Representative images of DA neurons (brown) from lateral (lat) and intermediate (int) subregions of the VTA in 3-month-old WT and Tg mice (scale: 10  $\mu$ m). The plots show soma area and perimeter of DA neurons (n = 4 mice per genotype). *Soma area*: Two-way ANOVA for Subregion vs Genotype: Interaction:  $F_{1,12} = 0.672$ ,  $p = 0.428$ ; Genotype:  $F_{1,12} = 0.023$ ,  $p = 0.882$ ; Subregion:  $F_{1,12} = 21.38$ ,  $p = 0.0006$ ; WT lat vs Tg lat:  $p = 0.900$ ; WT lat vs WT int:  $*p = 0.011$ ; WT lat vs Tg int:  $*p = 0.025$ ; Tg lat vs WT int:  $*p = 0.036$ ; Tg lat vs Tg int:  $p = 0.081$ ; WT int vs Tg int:  $p = 0.964$  with Tukey's post-hoc test. *Soma perimeter*: Two-way ANOVA: Interaction:  $F_{1,12} = 0.054$ ,  $p = 0.820$ ; Genotype:  $F_{1,12} = 0.110$ ,  $p = 0.746$ ; Subregion:  $F_{1,12} = 15.73$ ,  $p = 0.002$ ; WT lat vs Tg lat:  $p = 0.999$ ; WT lat vs WT int:  $p = 0.088$ ; WT lat vs Tg int:  $*p = 0.044$ ; Tg lat vs WT int:  $p = 0.098$ ; Tg lat vs Tg int:  $*p = 0.050$ ; WT int vs Tg int:  $p = 0.978$  with Tukey's test).

**C.** Same as in B but showing data from 6-month-old mice (n = 7 mice per genotype). *Soma area*: Two-way ANOVA for Subregion vs Genotype: Interaction:  $F_{1,24} = 9.283$ ,  $p = 0.006$ ; Genotype:  $F_{1,24} = 8.595$ ,  $p = 0.007$ ; Subregion:  $F_{1,24} = 13.39$ ,  $p = 0.0012$ ; WT lat vs Tg lat:  $**p = 0.002$ ; WT lat vs WT int:  $***p = 0.0004$ ; WT lat vs Tg int:  $***p = 0.0005$ ; Tg lat vs WT int:  $p = 0.955$ ; Tg lat vs Tg int:  $p = 0.972$ ; WT int vs Tg int:  $p = 0.999$  with Tukey's test. *Soma perimeter*: Two-way ANOVA:  $F_{1,24} = 8.403$ ,  $p = 0.008$ ; Genotype:  $F_{1,24} = 8.989$ ,  $p = 0.006$ ; Subregion:  $F_{1,24} = 6.992$ ,  $p = 0.014$ ; WT lat vs Tg lat:  $**p = 0.002$ ; WT lat vs WT int:  $**p = 0.003$ ; WT lat vs Tg int:  $**p = 0.003$ ; Tg lat vs WT int:  $p = 0.994$ ; Tg lat vs Tg int:  $p = 0.998$ ; WT int vs Tg int:  $p = 0.999$  with Tukey's test).

**D.** The plot shows stereological quantification of TH<sup>+</sup> cell numbers in the lateral VTA of WT and Tg mice at 3- and 6- months of age (3 months: n = 4 mice per genotype; 6 months: n = 7 mice per genotype). Two-way ANOVA for Age vs Genotype: Interaction:  $F_{1,18} = 0.220$ ,  $p = 0.645$ ; Age:  $F_{1,18} = 0.799$ ,  $p = 0.383$ ; Genotype:  $F_{1,18} = 5.127$ ,  $p = 0.036$ ; WT 3 m vs Tg 3 m:  $p = 0.679$ ; WT 3 m vs WT 6 m:  $p = 0.990$ ; WT 3 m vs Tg 6 m:  $p = 0.152$ ; Tg 3 m vs WT 6 m:  $p = 0.768$ ; Tg 3 m vs Tg 6 m:  $p = 0.771$ ; WT 6 m vs Tg 6 m:  $p = 0.143$  with Tukey's test).

performances in AD and PD models via autophagic degradation of A $\beta$  and  $\alpha$ -synuclein, respectively (Hebrun et al., 2018, 2013a; Lonskaya et al., 2014, 2013b).

To test the efficacy of this drug in blocking or delaying the functional deficits of DA neurons in Tg2576 mice, we intraperitoneally (i.p.) administered Nilotinib (1 mg kg<sup>-1</sup>) or vehicle on alternate days starting from 1.5 months of age (i.e. prior to cell death onset; see Supplementary Fig. 4A for treatment scheme).

First, to confirm that Nilotinib inhibits c-Abl activity in the midbrain of 3-month-old Tg2576 mice, we checked basal and phosphorylated levels of c-Abl upon drug treatment. Thus, we probed protein prepared from the midbrain of Tg2576 mice treated with vehicle or Nilotinib, using antibodies against c-Abl and its phosphorylated form. We found that Nilotinib reduced c-Abl phosphorylation in the midbrain from Tg2576 mice (Fig. 5A), while no changes were observed in basal c-Abl levels (Fig. 5A). Importantly, Nilotinib-treated Tg2576 mice showed a reduction of LC3II/LC3I ratio (Fig. 5A), suggesting that the drug can promote the autophagic clearance of the accumulated autophagosome vesicles in midbrain neurons. To investigate this further, we quantified the number and the dynamics of autophagic vesicles in 3-month-old Tg2576 mice injected with the AAV2/9-mCherry-GFP-LC3 construct and treated by vehicle or Nilotinib. Interestingly, in TH<sup>+</sup> neurons from Nilotinib-treated Tg2576 mice we observed a reduction of yellow puncta (Fig. 5B), suggestive of a reduced accumulation of autophagosome vesicles, while red puncta per cell remained unchanged. In strict compliance, the analysis of the dynamics of LC3 vesicles revealed an increased ratio (red/yellow puncta), thus confirming that the autophagosome clearance is improved with Nilotinib treatment (Fig. 5B, compare with Fig. 4D).

Since autophagy facilitates Amyloid Precursor Protein (APP) degradation and A $\beta$  clearance (Son et al., 2012; Zhou et al., 2011), we next assessed whether Nilotinib could reduce the A $\beta$  load in Tg2576 mice, at an age-point when no A $\beta$ -plaque were detected, as previously demonstrated (Nobili et al., 2017). By confocal microscopy we quantified the intracellular A $\beta$  load in VTA DA neurons and found that Nilotinib-treated Tg2576 mice showed decreased A $\beta$  levels when compared to control mice (vehicle-treated Tg2576; Fig. 5C; see Supplementary Fig. 4C for antibody specificity). Importantly, reduction in A $\beta$  levels was also observed in neurons from other brain regions, indicating a global effect of Nilotinib in Tg2576 mice (see Supplementary Fig. 4D).

### 3.5. Nilotinib prevents DA neuron degeneration in Tg2576 mice

Given the improvement in autophagy function and the reduction in the A $\beta$  load in VTA DA neurons of Tg2576 mice, we next analysed the firing properties, viability, and morphology of these neurons, to evaluate

the potential neuroprotective effect of Nilotinib.

Nilotinib treatment induced a significant functional improvement in 3-month-old Tg2576 DA neurons, evident as recovery of the spontaneous firing frequency (Fig. 6A). Importantly, stereological counting of DA neurons in 6-month-old mice confirmed that Nilotinib could protect these cells from degeneration (Fig. 6B). These data prove that, similarly to what observed in PD animals (Hebrun et al., 2013a; Karuppagounder et al., 2014), Nilotinib succeeds in preventing DA neuron degeneration also in Tg2576 mice.

Additional observations performed on age-matched WT mice showed that treatment with Nilotinib had no adverse effect on neuronal survival (Fig. 6B), and the drug was well-tolerated by the animals despite the long treatment regime, with no apparent differences on animal weight (Supplementary Fig. 4B).

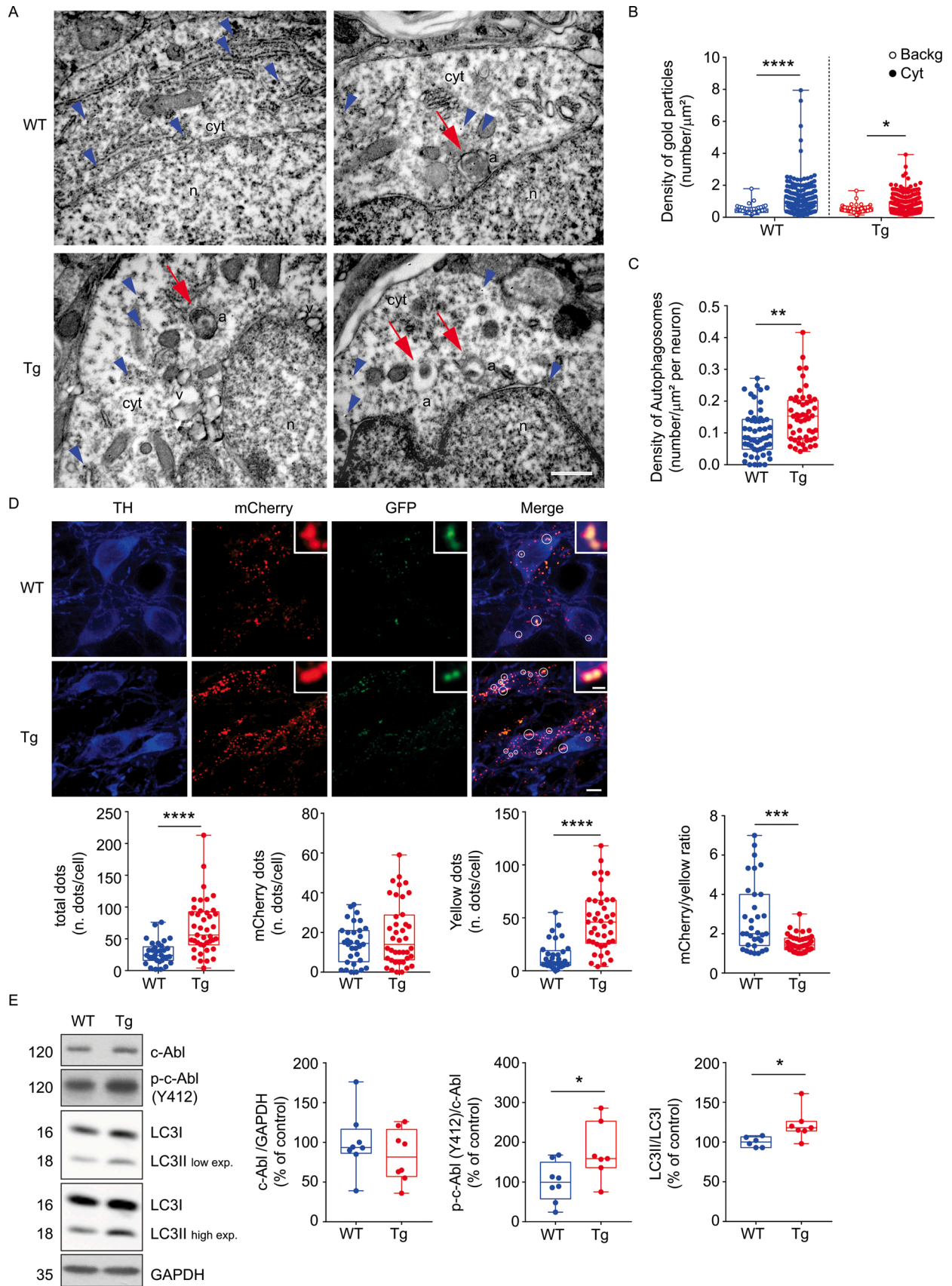
Of note, Nilotinib treatment could also prevent the alterations in soma area and perimeter of lateral DA neurons in Tg2576 mice (Fig. 6C), which are indicative of neurodegeneration. Conversely, Nilotinib had no effect in the DA neurons of the intermediate subfield of the VTA, where no morphological differences were observed between WT and Tg2576 neurons (Supplementary Fig. 4E, see also Fig. 3C).

### 3.6. Nilotinib prevents memory deficits in 6-month-old Tg2576 mice

VTA degeneration in Tg2576 mice results in lower DA innervation in the dorsal hippocampus, leading to lower DA outflow (Cordella et al., 2018; Nobili et al., 2017). We had previously demonstrated that this reduction in DA levels was associated with deficits in pyramidal neuron excitability and synaptic plasticity, and with dysfunctional hippocampal-related memory performance in Tg2576 mice. All these deficits could be rescued by systemic treatment with the DA precursor levodopa (Cordella et al., 2018; Nobili et al., 2017).

Given that Nilotinib treatment prevented the degeneration of DA neurons of the VTA in Tg2576 mice, we wondered whether this effect could be translated as recovery of hippocampal DA levels. Indeed, microdialysis experiments on freely-moving animals showed that the chronic Nilotinib administration increased the DA tone in 6 month-old Tg2576 mice compared to vehicle-treated ones (Fig. 6D), in line with the neuroprotective effect exerted on DA neurons.

DA release in the hippocampus promotes spatial memory, reward-associated memory, novel-object recognition and memory consolidation (Broussard et al., 2016; Kempadoo et al., 2016; Mamad et al., 2017; McNamara et al., 2014; Rosen et al., 2015; Rossato et al., 2009; Takeuchi et al., 2016). Thus, we asked whether the impaired memory function observed in Tg2576 mice could be ameliorated by Nilotinib treatment. To test different phases of learning and memory in mice, we performed the Novel Object Recognition Test (NORT) given the repeatedly demonstrated defects in object recognition memory of Tg2576 mice



(caption on next page)

**Fig. 4.** Autophagy changes in DA neurons of the VTA from 3-month-old Tg2576 mice.

- A.** TEM images of TH<sup>+</sup> neurons from post-embedded VTA of 3-month-old WT and Tg mice. The blue arrowheads point to TH gold particles (18 nm) in the cytoplasm (cyt) of neurons. Red arrows indicate representative autophagosomes (a) with degraded amorphous electron dense material (arrow in WT and in the first microscopic field of Tg), and with mixed electron dense and electron translucent contents (arrows in the second field of Tg); n, nucleus; v, vacuole (scale: 300 nm).
- B.** The plots show density of gold particles illustrating that in TH<sup>+</sup> neurons the cytoplasmic density is significantly higher than that of background (backg; WT: n = 53 neurons sampled for background level; 268 cytoplasmic TEM fields, 3 mice; Tg: n = 51 neurons sampled for background, 269 cytoplasmic TEM fields, 3 mice; Mann-Whitney tests for WT \*\*\*\*p < 0.0001, for Tg \*p = 0.016).
- C.** Density of autophagosomes showing increased numbers per  $\mu\text{m}^2$  in Tg neurons (n = 53 WT and 51 Tg neurons, from 3 mice per genotype; Mann-Whitney test \*\*p = 0.0013).
- D.** Analysis of confocal Z-stack triple immunofluorescent labelling for TH (blue), mCherry (red) and GFP (green) LC3 puncta in VTA coronal sections from 3-month-old WT and Tg mice (scale: 5  $\mu\text{m}$ ). Inserts show high magnification of single dots (scale bar: 1  $\mu\text{m}$ ). Box and whisker plots show the quantification of total (WT: n = 33 cells, Tg: n = 41 cells; 3 mice per genotype; Mann-Whitney test \*\*\*\*p < 0.0001), red, and yellow puncta (merge of red and green, indicated by white circles) dots per TH<sup>+</sup> cell (WT: n = 32 cells, Tg: n = 40 cells; 3 mice per genotype; mCherry: Mann-Whitney test p = 0.402; yellow: Mann-Whitney test \*\*\*\*p < 0.0001) and mCherry/yellow ratio (WT: n = 33 cells, Tg: n = 41 cells; 3 mice per genotype; Mann-Whitney test \*\*\*p < 0.001).
- E.** Representative western blot from the midbrain of 3-month-old WT and Tg mice and plots showing the levels (expressed as % of WT) of total c-Abl normalized to GAPDH used as loading control (n = 8 mice per genotype; Unpaired t-test, p = 0.370), p-c-Abl(Y412)/c-Abl (n = 8 WT and 7 Tg mice; Unpaired t-test, \*p = 0.039) and LC3II/LC3I ratio (WT: n = 6; Tg: n = 7 mice; Welch t-test, \*p = 0.025).

(Corsetti et al., 2020; Tagliatalata et al., 2009). During the training session, mice were left to freely explore two identical objects. Irrespective of genotype and treatment, all animals spent equal amounts of time with the objects, showing no preference for a given object (Supplementary Fig. 4F). During the test sessions, performed 1 and 24 h after training, the exposure to a novel object resulted in a significant increase in the time spent for its exploration for vehicle-treated and Nilotinib-treated WT animals, but not for vehicle-treated Tg2576 mice. Importantly, Nilotinib-treated Tg2576 mice behaved similarly to WT animals, showing no deficits in novel object recognition memory (Fig. 6E). No significant differences were found in the number of defecation boluses, indicating similar emotional reactivity in all mice (Supplementary Fig. 4G). Thus, we conclude that the neuroprotective effect of Nilotinib on DA neurons can prevent memory deficits by increasing the availability of DA in the hippocampus of Tg2576 mice.

#### 4. Discussion

We report here that the Tg2576 mouse model of AD exhibits early alterations in the function, morphology and autophagic process of VTA dopaminergic neurons. These deficits temporally coincide with the onset of neuronal degeneration (3 months; Nobili et al., 2017), and worsen with age. Importantly, they are associated with increased c-Abl activation via phosphorylation at residue Y412 and can be prevented by an early-starting chronic treatment with Nilotinib. Indeed, Nilotinib can improve autophagy, reduce the levels of A $\beta$ , and prevent the degeneration of Tg2576 DA neurons in the VTA, resulting in a rescue of DA levels in the hippocampus and in improvements in novel object recognition memory.

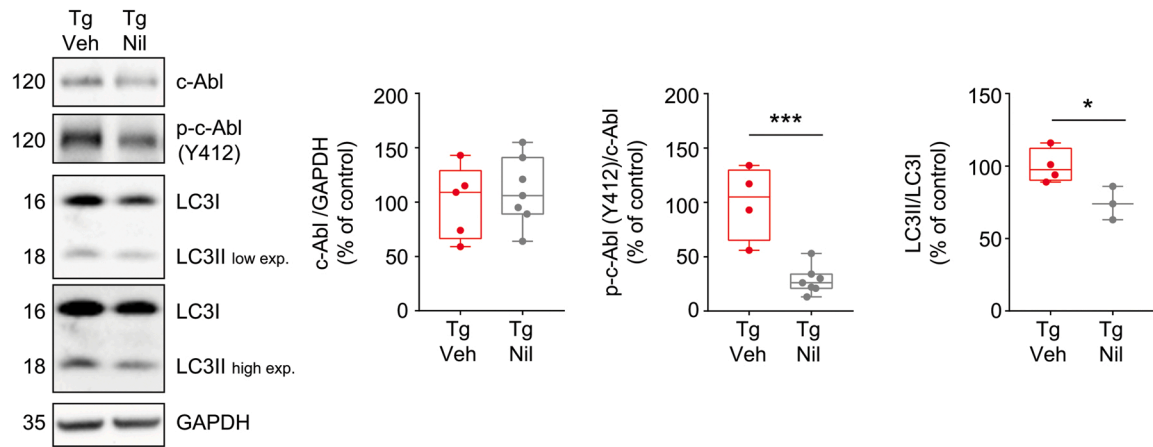
The present data confirm the hypothesis that multiple functional alterations in Tg2576 DA neurons contribute to cell vulnerability and eventually lead to progressive degeneration and overt cognitive and non-cognitive deficits in older animals (Cordella et al., 2018; Nobili et al., 2017). These functional deficits include increased spontaneous firing, increased excitability in response to depolarizing currents, and subtle changes in underlying neuronal conductances. The increased firing of Tg2576 DA neurons starts at 3 months of age since younger animals show normal neuronal function, and it becomes steeply pronounced at 6 months of age, suggesting that DA neuron firing rates increase along with disease progression. Many factors could contribute to the increased firing of DA neurons, including our evidence of a slight reduction in the K<sup>+</sup>-underlying SK-mediated conductance that would be compatible with increased excitability and reduced after-hyperpolarisation (Iyer et al., 2017; Ji et al., 2009). However, lack of changes in SK current densities and lack of changes in the regularity of firing (Ji and Shepard, 2006; Waroux et al., 2005) show that differences, if any, between genotypes are too small to be detectable. Alternatively, the hyper-excitable state of DA neurons could be a compensatory

mechanism to oppose the reduction of DA outflow to the projection areas (Nobili et al., 2017; see also Fig. 6D) via enhancement of DA-loading of synaptic vesicles (Aguilar et al., 2017). Changes in cell excitability might also be a direct or indirect effect of the increased A $\beta$  load in Tg2576 neurons (Ciccone et al., 2019) or of the observed autophagy impairment on voltage-gated Na<sup>+</sup> and/or K<sup>+</sup> conductances (Lieberman et al., 2020; Subramaniam et al., 2014). Nonetheless, although the mechanisms linking the hyper-excitable state with degeneration in Tg2576 DA neurons remain to be defined, the increased firing of these neurons might constitute one of the first acquired pathophysiological stages of the dopaminergic system in AD, right at the onset of midbrain neurodegeneration. Indeed, it is likely that this picture in Tg2576 mice is symmetrical to what many studies have described in PD models, referring to the 'stressful pacemaker theory' (Chan et al., 2009; Sulzer, 2007), whereupon enhancement of spontaneous firing and delayed action potential repolarization of substantia nigra DA neurons could contribute to PD progression by enhancing activity-dependent Ca<sup>2+</sup> loading and oxidative stress.

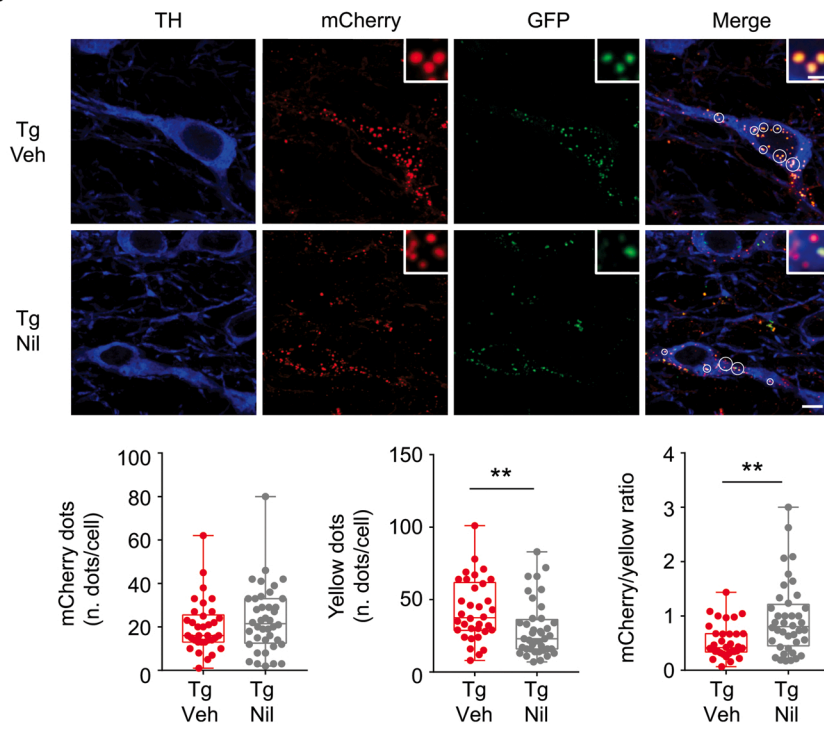
Importantly, the above-mentioned functional changes observed in 3-month-old Tg2576 mice coincide with the autophagy impairment observed with western blotting, electron and confocal microscopy. Autophagy is a catabolic process crucial for neuronal survival as it prevents the accumulation of unfolded proteins or damaged organelles, including mitochondria (Cavallucci et al., 2013a, 2013b; Nixon, 2013; Nobili et al., 2016; Viscomi and D'Amelio, 2012). Moreover, the higher pacemaker activity and massive axonal arborization of Tg2576 DA neurons could contribute to their vulnerability, because of the high metabolic demand and need of increased mitochondrial efficiency (Giguère et al., 2018; Krashia et al., 2019b). Indeed, TEM analysis on post-mortem AD brains revealed the presence of accumulated autophagic vacuoles in dystrophic neurites that are surrounded by neuronal fibrillary tangles (Nixon et al., 2005; Nixon and Cataldo, 2006), and similar evidence have been also found in AD models (Yang et al., 2011; Yu et al., 2005), although none of these studies have been performed on DA neurons. Here, in the Tg2576 mouse model of AD, we observed an increased accumulation of autophagosomes in 3-month-old DA neurons, suggesting an alteration in the autophagic mechanism. The accumulation of autophagosomes in Tg2576 DA neurons might be due to either an increase in their production or to a shortfall in the process of fusion with the endosomal-lysosomal system (Berg et al., 1998; De Duve and Wattiaux, 1966; Klionsky et al., 2021). Our TEM and confocal microscopy data suggest that in Tg2576 mice the alteration of the autophagic flux is likely not due to a block in the autophagosome-lysosome fusion; instead, the autophagosome accumulation would suggest that their clearance mechanism in Tg2576 neurons is less able to compensate for an increased production, leading to an imbalance in the autophagic flux.

Although the earliest effects on DA neurons we could detect in Tg2576 mice were the above-mentioned functional and autophagic

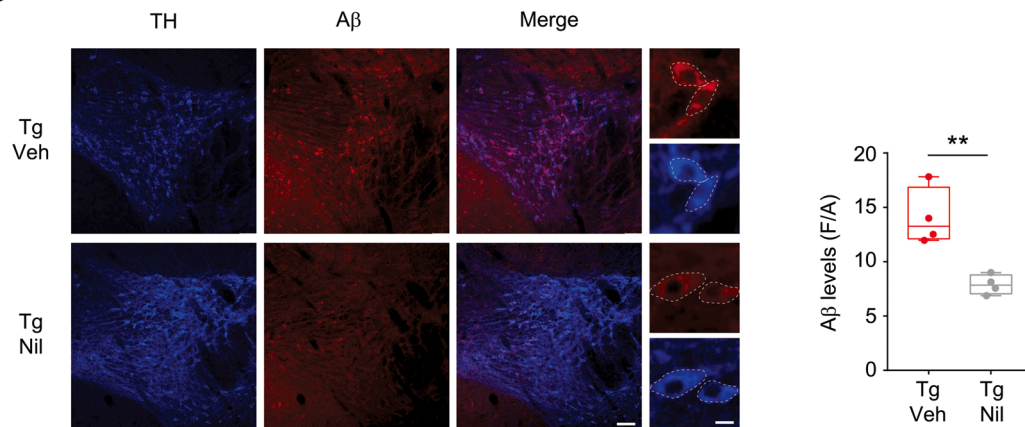
A



B



C



(caption on next page)

**Fig. 5.** Nilotinib ameliorates autophagy alterations in Tg2576 mice.

**A.** Representative western blot from the midbrain of 3-month-old Tg mice after treatment with either vehicle (Veh) or Nilotinib (Nil) and plots showing the levels (expressed as % of Tg Veh) of total c-Abl normalized to GAPDH used as loading control (Tg Veh: n = 5; Tg Nil: n = 7 mice; Unpaired *t*-test, *p* = 0.603), as well as p-c-Abl(Y412)/c-Abl (Tg Veh: n = 5; Tg Nil: n = 7 mice; Unpaired *t*-test, \*\*\**p* < 0.001) and LC3II/LC3I ratio (Tg Veh: n = 4; Tg Nil: n = 3 mice; Unpaired *t*-test, \**p* = 0.034).

**B.** Analysis of confocal Z-stack triple immunofluorescent labelling for TH (blue), mCherry (red) and GFP (green) LC3 puncta in VTA coronal sections from 3-month-old Tg mice after treatment with either Veh or Nil (scale: 5 μm). Inserts show high magnification of single dots (scale bar: 1 μm). Box and whisker plots show the quantification of red and yellow puncta (merge of red and green, indicated by white circles) dots per TH<sup>+</sup> cell (Tg Veh: n = 34 cells, Tg Nil: n = 40 cells; 3 mice per treatment; *mCherry*: Mann-Whitney test, *p* = 0.321; *yellow*: Mann-Whitney test, \*\**p* = 0.002) and mCherry/yellow ratio (Tg Veh: n = 34 cells, Tg Nil: n = 40 cells; 3 mice per treatment; Mann-Whitney test, \*\**p* = 0.004).

**C.** Analysis of confocal Z-stack double immunofluorescent labelling for TH (blue) and Aβ (red) in VTA coronal sections from 3-month-old Tg mice after treatment with either Veh or Nil (scale: 50 μm). Inserts show high magnification of single cells (scale: 15 μm). Box and whisker plots show the quantification of Aβ signal in VTA TH<sup>+</sup> neurons (n = 4 mice per treatment; Unpaired *t*-test, \*\**p* = 0.004).

deficits, we also observed age-dependent morphological changes in DA neurons, with both soma area and perimeter being reduced in 6-month-old Tg2576 mice. Surprisingly, this effect was only evident in lateral VTA neurons, whereas cells in the intermediate VTA were unaltered. Our data could suggest that lateral neurons undergo shrinkage and/or that larger neurons degenerate. In fact, stereological counting showed a trend towards DA neuron reduction in the lateral subfield of the VTA, although this result was not significant, suggesting that the overall ~40% reduction of DA neurons in 6-month-old Tg2576 mice (Nobili et al., 2017) is the result of degeneration in more than one single subregion (see also Fig. 6B). Neuronal death in the central nervous system has always been an arduous process to decipher and cell shrinkage is considered one of the main morphological features of apoptosis (Bortner and Cidlowski, 2002). Although the relationship between neuronal shrinkage and apoptosis has been neglected for decades, several studies show that it is a challenging area of study, particularly with regard to its relation with signal transduction pathways, cellular metabolism, and gene expression (Bortner and Cidlowski, 1998; McCarthy and Cotter, 1997). The mechanisms leading to cell shrinkage in a specific VTA subregion remain obscure, and further studies are needed to identify the intracellular and extracellular stimuli related to this event. Yet, considering that cell shrinkage is a hallmark of a specific VTA subregion, a more detailed investigation of the interplay between the morphological features of a given neuron and the area to which it projects would be of great interest, particularly given the high heterogeneity of VTA DA neurons (Lammel et al., 2008; Margolis et al., 2008; Roeper, 2013).

Of note, in line with the changes in the autophagic process in Tg2576 DA neurons, we observed an increase in the phosphorylated form of c-Abl in the midbrain at 3 months of age. Interestingly, the increase in phospho-c-Abl appears to be restricted to the midbrain whereas c-Abl phosphorylation levels and autophagy activity remain unchanged in other brain regions that are particularly relevant to the disease (hippocampus, amygdala, and cortex). c-Abl is an important regulator of the autophagic process (Abushouk et al., 2018) and of other pathways that set the choice between survival and cell death, thus the observation of an increase in c-Abl phosphorylation in Tg2576 mice is consistent with other studies that identify c-Abl as a pathogenesis mediator in AD (Alvarez et al., 2004; Jing et al., 2009).

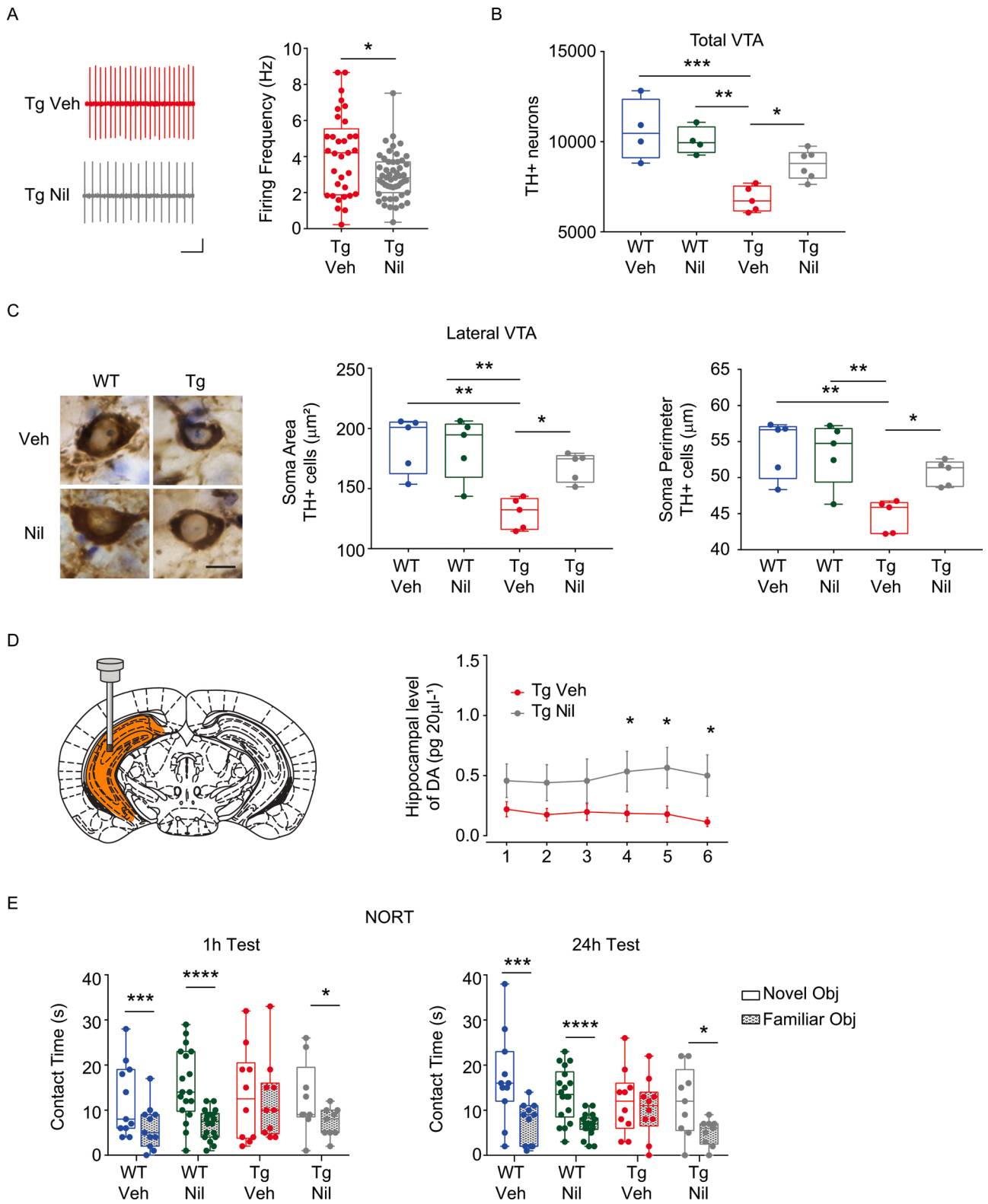
Importantly, the present data show that treatment of Tg2576 mice with Nilotinib can reduce the activation of c-Abl in DA neurons, thus improving the autophagy activity and Aβ clearance. Closely related to these events, Nilotinib prevents the loss as well as the functional and morphological alterations of DA neurons. Moreover, Nilotinib treatment prevents the reduction of DA levels in the hippocampus of Tg2576 mice and the memory deficits related to novel object recognition. These data are in strict compliance with numerous other studies demonstrating that c-Abl inhibitors, like Nilotinib, have exceptionally positive effects in PD mouse models. Indeed, it was shown that Nilotinib is able to cross the blood-brain barrier, degrade α-synuclein via autophagy, prevent DA neuron loss and improve motor and cognitive behaviour (Hebron et al., 2018, 2014, [Hebron et al., 2013a] 2013a, 2013b; Imam et al., 2011; Karuppagounder et al., 2014; Ko et al., 2010; Lonskaya et al., 2015,

2014, [Lonskaya et al., 2013b] 2013b, 2013a; Mahul-Mellier et al., 2014). Of note, the recovery of DA levels in the hippocampus, and the improvement of hippocampal memory functions observed in Nilotinib-treated Tg2576 mice, is highly compatible with the direct neuro-protective effect of the drug on the survival of midbrain DA neurons. However, we cannot exclude that the beneficial effect of the drug might also involve additional brain regions. Indeed, Nilotinib evoked a global reduction of Aβ levels on all the brain areas we checked. On the other hand, we are fairly confident that cognitive impairments in our Tg2576 model, at least until 6 months of age, are not related to dysfunctions in other DA-releasing neurons such as those in the locus coeruleus, given that this nucleus still appears to be intact and the levels of noradrenaline in the hippocampus are normal (Nobili et al., 2017). This of course does not exclude that in a more advanced stage of the disease (Guérin et al., 2009; Krashia et al., 2019b; Liu et al., 2008), reduced DA release from locus coeruleus neurons to the hippocampus could worsen DA-related cognitive functions.

Our experiments do not permit to discern how the levels of phosphorylated c-Abl are increased in the midbrain of Tg2576 mice or what the precise mechanism linking c-Abl with the selective degeneration of DA neurons is. Additionally, whether the selective degeneration at 3 months of age starts locally in the midbrain and/or is the result of a dying-back mechanism starting from the axonal terminals (Liu et al., 2008; Moreno-Castilla et al., 2016), is yet to be defined. Nonetheless, we can affirm that, at the early stage of the disease, among all the brain areas we studied, only the midbrain shows alterations in c-Abl activity and autophagy, two factors relevant to degeneration. In the same line of thinking, the intracellular accumulation of Aβ *per se* does not appear to be sufficient to induce cell death in the other brain regions we studied, at least at this age-point. Thus, we can hypothesize that the selective degeneration of VTA DA neurons at 3 months of age might be due to the cumulative effect of various insults to the neuron (such as increased phospho-c-Abl, autophagic deficits, Aβ accumulation and/or oxidative stress), making these cells more susceptible than others to degeneration. In line with our hypothesis, the combined reduction of Aβ and phospho-c-Abl levels, together with the rescue of the autophagic flow in Tg2576 DA neurons treated with Nilotinib, is particularly effective in preventing degeneration. Of note, the positive effect of Nilotinib on DA neuron survival in our AD mice is particularly relevant given that at doses lower than the FDA-approved ones for chronic myeloid leukemia (Deremer et al., 2008; Mahon et al., 2008; Skorski, 2011), the drug can reduce disease-related biomarkers in phase-2 clinical trials – including amyloid levels and hippocampal volume in AD patients and α-synuclein levels in PD patients (Pagan et al., 2016, 2019; Turner et al., 2020)

## 5. Conclusions

Our data confirm the very recent clinical evidence from MCI and AD patients showing that functional, structural and metabolic changes affecting the VTA and its projection areas in the mesocorticolimbic pathway occur at the earlier stages of the disease (De Marco and Venneri, 2018; Iaccarino et al., 2020; Serra et al., 2018). These preclinical



(caption on next page)

**Fig. 6.** Nilotinib prevents DA neuron loss and memory deficits in Tg2576 mice.

**A.** Sample traces showing the spontaneous firing recorded from DA neurons in the VTA of Tg mice of 3 months of age after treatment with either Veh or Nil (scale: 1 s; 0.2 mV). The graph indicates mean firing frequency (Tg Veh:  $n = 33$  neurons, Tg Nil:  $n = 51$  neurons, 3 mice per treatment; Mann-Whitney test  $*p = 0.016$ ).

**B.** The plot shows stereological quantification of total TH<sup>+</sup> cell numbers in the VTA of 6-month-old mice treated with Veh or Nil (WT Veh:  $n = 4$  mice; WT Nil:  $n = 4$  mice; Tg Veh:  $n = 5$  mice; Tg Nil:  $n = 6$  mice; Two-Way ANOVA for Genotype vs Treatment: Interaction:  $F_{1,15} = 6.849$ ,  $p = 0.019$ ; Genotype:  $F_{1,15} = 29.47$ ,  $p < 0.0001$ ; Treatment:  $F_{1,15} = 1.914$ ,  $p = 0.187$ ; WT Veh vs WT Nil:  $p = 0.966$ ; WT Veh vs Tg Veh:  $***p = 0.0003$ ; WT Veh vs Tg Nil:  $p = 0.062$ ; WT Nil vs Tg Veh:  $**p = 0.002$ ; WT Nil vs Tg Nil:  $p = 0.313$ ; Tg Veh vs Tg Nil:  $*p = 0.045$  with Sidak's post-hoc test).

**C.** Representative images of DA neurons (brown) from the lateral VTA in 6-month-old treated WT and Tg mice (scale bar: 10  $\mu\text{m}$ ). The plots show soma area and perimeter of TH<sup>+</sup> neurons in the lateral VTA ( $n = 5$  mice per group). *Soma area*: Two-Way ANOVA for Genotype vs Treatment: Interaction:  $F_{1,16} = 5.984$ ,  $p = 0.026$ ; Genotype:  $F_{1,16} = 4.362$ ,  $p = 0.053$ ; Treatment:  $F_{1,16} = 18.52$ ,  $p = 0.0005$ ; WT Veh vs WT Nil:  $p = 0.994$ ; WT Veh vs Tg Veh:  $**p = 0.001$ ; WT Veh vs Tg Nil:  $p = 0.424$ ; WT Nil vs Tg Veh:  $**p = 0.002$ ; WT Nil vs Tg Nil:  $p = 0.568$ ; Tg Veh vs Tg Nil:  $*p = 0.026$ , with Tukey's post-hoc test. *Soma perimeter*: Interaction:  $F_{1,16} = 5.375$ ,  $p = 0.034$ ; Genotype:  $F_{1,16} = 3.448$ ,  $p = 0.082$ ; Treatment:  $F_{1,16} = 17.78$ ,  $p = 0.001$ ; WT Veh vs WT Nil:  $p = 0.988$ ; WT Veh vs Tg Veh:  $**p = 0.002$ ; WT Veh vs Tg Nil:  $p = 0.371$ ; WT Nil vs Tg Veh:  $**p = 0.003$ ; WT Nil vs Tg Nil:  $p = 0.551$ ; Tg Veh vs Tg Nil:  $*p = 0.042$  with Tukey's).

**D.** Anatomical position of the microdialysis probe in the mouse hippocampus, corresponding to AP  $-3.0$ , ML  $\pm 2.7$  from bregma. Probe length was 5 mm. The plot shows DA levels in the hippocampus of 6-month-old Tg mice treated with Veh or Nil measured during microdialysis *in-vivo*. Data represent mean ( $\pm$  s.e.m.) of DA levels of six consecutive dialysate samples collected every 20 min (Tg Veh:  $n = 6$  mice; Tg Nil:  $n = 5$  mice. Two-Way ANOVA for Time vs Treatment: Interaction:  $F_{5,45} = 3.038$ ,  $p = 0.019$ ; Time:  $F_{5,45} = 1.936$ ,  $p = 0.107$ ; Treatment:  $F_{1,9} = 3.881$ ,  $p = 0.080$ ; *Time 1*: Unpaired *t*-test:  $p = 0.135$ ; *Time 2*: Unpaired *t*-test:  $p = 0.104$ ; *Time 3*: Unpaired *t*-test:  $p = 0.189$ ; *Time 4*: Mann-Whitney test:  $*p = 0.030$ ; *Time 5*: Unpaired *t*-test:  $*p = 0.050$ ; *Time 6*: Unpaired *t*-test:  $*p = 0.040$ ).

**E.** Plots show the contact time (s) spent by mice with the novel or familiar object during the Novel Object Recognition Test (NORT) sessions at 1 h and 24 h after training (*1 h*: WT Veh:  $n = 11$  mice,  $***p = 0.001$ ; WT Nil:  $n = 18$  mice,  $****p < 0.0001$ ; Tg Veh:  $n = 10$  mice,  $p = 0.364$ ; Tg Nil:  $n = 9$  mice,  $*p = 0.028$ , all with paired *t*-test; *24 h*: WT Veh:  $n = 11$  mice,  $***p = 0.0007$ ; WT Nil:  $n = 18$  mice,  $****p < 0.0001$ ; Tg Veh:  $n = 10$  mice,  $p = 0.200$ ; Tg Nil:  $n = 9$  mice,  $*p = 0.016$  with paired *t*-test).

findings suggest that pharmacological interventions targeting the mesocorticolimbic system, such as Nilotinib treatment, would have better chances of succeeding if started at the earliest stage of diagnosed MCI, to prevent the earliest effects occurring onto DA neurons of the VTA.

## 6. Author contributions

M.D.A. conceived and designed the study; L.L.B., A.N. and M.T.V. designed and carried out cell counting, morphological analysis, immunohistochemistry and immunofluorescence experiments; L.L.B., A.N. P. K. and F.V. designed and carried out animal Nilotinib treatments; L.L.B. and E.C. designed and carried out the molecular biology experiments; P. K. designed and carried out stereotaxic injections; F.V., E.S. designed and carried out the electrophysiological experiments; P.K. and N.B.M supervised the electrophysiological experiments; F.C. and M.M. designed, performed and analyzed electron microscopy experiments; S. P.A. and E.C.L. designed, performed and analyzed microdialysis experiments; D.C. and L.P. designed, performed and analyzed behavioral experiments; M.D.A., L.L.B., F.V., P.K., and A.N. wrote the manuscript. All authors discussed results and commented on the manuscript.

## 7. Funding

M.D.A. was supported by the Americanthe US Alzheimer's Association (USA) (AARG-18-566270), by the Italian Ministry of Health (IT) (Research Grant: RF-2018-12365527) and by Fondazione Roma (Rome, Italy). N.B.M. was supported by the Italian Ministry of Health (Research Grant: RF-2018-12365509). F.C. was supported by the Italian Ministry of University and Research (IT) (PRIN 2015H4K2CR) and by UNIVPM University (IT) Funding (PSA 2017). S.P.A. was supported by Sapienza University of Rome (IT) (University Funding: Ateneo 2016). E.C.L. was supported by the Italian Ministry of Health (Young Researcher Grant: GR-2018-12365991). A.N. was supported by a post-doctoral Fellowship by Collegio Ghislieri (Pavia, Italy).

## Acknowledgements

The AAV2/9-mCherry-GFP-LC3 viral particles used in this study were a kind gift from Dr Benjamin Dehay (Univ. of Bordeaux, France).

We thank Drs Riviello and Wirz for assistance with animal caring.

## Appendix A. The Peer Review Overview and Supplementary data

Supplementary data associated with this article can be found, in the online version, at doi:<https://doi.org/10.1016/j.pneurobio.2021.102031>.

## References

- Abushouk, A.I., Negida, A., Elshenawy, R.A., Zein, H., Hammad, A.M., Menshaw, A., Mohamed, W.M.Y., 2018. C-abl inhibition; a novel therapeutic target for parkinson's disease. *CNS Neurol. Disord. Drug Targets* 17, 14–21. <https://doi.org/10.2174/1871527316666170602101538>.
- Aguilar, J.I., Dunn, M., Mingote, S., Karam, C.S., Farino, Z.J., Sonders, M.S., Choi, S.J., Grygoruk, A., Zhang, Y., Cela, C., Choi, B.J., Flores, J., Freyberg, R.J., McCabe, B.D., Mosharov, E.V., Krantz, D.E., Javitch, J.A., Sulzer, D., Sames, D., Rayport, S., Freyberg, Z., 2017. Neuronal depolarization drives increased dopamine synaptic vesicle loading via VGLUT. *Neuron* 95, 1074–1088. <https://doi.org/10.1016/j.neuron.2017.07.038> e7.
- Allard, P., Alafuzoff, I., Carlsson, A., Eriksson, K., Ericson, E., Gottfries, C.G., Marcusson, J.O., 1990. Loss of dopamine uptake sites labeled with [3H]GBR-12935 in Alzheimer's disease. *Eur. Neurol.* 30, 181–185. <https://doi.org/10.1159/000117341>.
- Alvarez, A.R., Sandoval, P.C., Leal, N.R., Castro, P.U., Kosik, K.S., 2004. Activation of the neuronal c-Abl tyrosine kinase by amyloid-beta-peptide and reactive oxygen species. *Neurobiol. Dis.* 17, 326–336. <https://doi.org/10.1016/j.nbd.2004.06.007>.
- Alves, G.S., Carvalho, A.F., de Amorim de Carvalho, L., Sudo, F.K., Siqueira-Neto, J.I., Oertel-Knochel, V., Jurcoane, A., Knochel, C., Boecker, H., Laks, J., Pantel, J., 2017. Neuroimaging findings related to behavioral disturbances in alzheimer's disease: a systematic review. *Curr. Alzheimer Res.* 14, 61–75. <https://doi.org/10.2174/1567205013666160603010203>.
- Ambrée, O., Richter, H., Sachser, N., Lewejohann, L., Dere, E., de Souza Silva, M.A., Herring, A., Keyvani, K., Paulus, W., Schäbitz, W.-R., 2009. Levodopa ameliorates learning and memory deficits in a murine model of Alzheimer's disease. *Neurobiol. Aging* 30, 1192–1204. <https://doi.org/10.1016/j.neurobiolaging.2007.11.010>.
- Bardgett, M.E., Davis, N.N., Schultheis, P.J., Griffith, M.S., 2011. Ciproxifan, an H3 receptor antagonist, alleviates hyperactivity and cognitive deficits in the APPTg2576 mouse model of alzheimer's disease. *Neurobiol. Learn. Mem.* 95, 64–72. <https://doi.org/10.1016/j.nlm.2010.10.008>.
- Berg, T.O., Fengsrud, M., Strømhaug, P.E., Berg, T., Seglen, P.O., 1998. Isolation and characterization of rat liver amphisomes. Evidence for fusion of autophagosomes with both early and late endosomes. *J. Biol. Chem.* 273, 21883–21892. <https://doi.org/10.1074/jbc.273.34.21883>.
- Bethus, I., Tse, D., Morris, R.G.M., 2010. Dopamine and memory: modulation of the persistence of memory for novel hippocampal NMDA receptor-dependent paired associates. *J. Neurosci.* 30, 1610–1618. <https://doi.org/10.1523/JNEUROSCI.2721-09.2010>.
- Björklund, A., Dunnett, S.B., 2007. Dopamine neuron systems in the brain: an update. *Trends Neurosci.* 30, 194–202. <https://doi.org/10.1016/j.tins.2007.03.006>.
- Bortner, C.D., Cidlowski, J.A., 1998. A necessary role for cell shrinkage in apoptosis. *Biochem. Pharmacol.* 56, 1549–1559. [https://doi.org/10.1016/s0006-2952\(98\)00225-1](https://doi.org/10.1016/s0006-2952(98)00225-1).
- Bortner, C.D., Cidlowski, J.A., 2002. Apoptotic volume decrease and the incredible shrinking cell. *Cell Death Differ.* 9, 1307–1310. <https://doi.org/10.1038/sj.cdd.4401126>.

- Braak, H., Bohl, J.R., Müller, C.M., Rüb, U., Vos, R.A., Ide, Tredici, K.D., 2006. Stanley Fahn Lecture 2005: the staging procedure for the inclusion body pathology associated with sporadic Parkinson's disease reconsidered. *Mov. Disord.* 21, 2042–2051. <https://doi.org/10.1002/mds.21065>.
- Broussard, J.I., Yang, K., Levine, A.T., Tsetsenis, T., Jenson, D., Cao, F., Garcia, I., Arenkiel, B.R., Zhou, F.-M., De Biasi, M., Dani, J.A., 2016. Dopamine regulates aversive contextual learning and associated in vivo synaptic plasticity in the Hippocampus. *Cell Rep.* 14, 1930–1939. <https://doi.org/10.1016/j.celrep.2016.01.070>.
- Caligiore, D., Silveti, M., D'Amelio, M., Puglisi-Allegra, S., Baldassarre, G., 2020. Computational modeling of catecholamines dysfunction in Alzheimer's disease at pre-plaque stage. *J. Alzheimers Dis. JAD* 77, 275–290. <https://doi.org/10.3233/JAD-200276>.
- Cancino, G.I., Toledo, E.M., Leal, N.R., Hernandez, D.E., Yévenes, L.F., Inestrosa, N.C., Alvarez, A.R., 2008. STI571 prevents apoptosis, tau phosphorylation and behavioural impairments induced by Alzheimer's beta-amyloid deposits. *Brain* 131, 2425–2442. <https://doi.org/10.1093/brain/awn125>.
- Cancino, G.I., Perez de Arce, K., Castro, P.U., Toledo, E.M., von Bernhard, R., Alvarez, A.R., 2011. c-Abl tyrosine kinase modulates tau pathology and Cdk5 phosphorylation in AD transgenic mice. *Neurobiol. Aging* 32, 1249–1261. <https://doi.org/10.1016/j.neurobiolaging.2009.07.007>.
- Canter, R.G., Penney, J., Tsai, L.-H., 2016. The road to restoring neural circuits for the treatment of Alzheimer's disease. *Nature* 539, 187–196. <https://doi.org/10.1038/nature20412>.
- Castillo, K., Valenzuela, V., Matus, S., Nassif, M., Oñate, M., Fuentealba, Y., Encina, G., Irrazabal, T., Parsons, G., Court, F.A., Schneider, B.L., Armentano, D., Hetz, C., 2013. Measurement of autophagy flux in the nervous system in vivo. *Cell Death Dis.* 4, e917. <https://doi.org/10.1038/cddis.2013.421>.
- Cavallucci, V., Berretta, N., Nobili, A., Nisticò, R., Mercuri, N.B., D'Amelio, M., 2013a. Calcineurin inhibition rescues early synaptic plasticity deficits in a mouse model of Alzheimer's disease. *Neuromolecular Med.* 15, 541–548. <https://doi.org/10.1007/s12017-013-8241-2>.
- Cavallucci, V., Ferraina, C., D'Amelio, M., 2013b. Key role of mitochondria in Alzheimer's disease synaptic dysfunction. *Curr. Pharm. Des.* 19, 6440–6450. <https://doi.org/10.2174/1381612811319360005>.
- Chan, C.S., Gertler, T.S., Surmeier, D.J., 2009. Calcium homeostasis, selective vulnerability and Parkinson's disease. *Trends Neurosci.* 32, 249–256. <https://doi.org/10.1016/j.tins.2009.01.006>.
- Chan, C.S., Gertler, T.S., Surmeier, D.J., 2010. A molecular basis for the increased vulnerability of substantia nigra dopamine neurons in aging and Parkinson's disease. *Mov. Disord.* 25 (Suppl 1), S63–70. <https://doi.org/10.1002/mds.22801>.
- Chételat, G., 2013. Alzheimer disease:  $\beta$ -independent processes—rethinking preclinical AD. *Nat. Rev. Neurol.* 9, 123–124. <https://doi.org/10.1038/nrneuro.2013.21>.
- Ciccone, R., Franco, C., Piccialli, I., Boscia, F., Casamassa, A., de Rosa, V., Cepparulo, P., Cataldi, M., Annunziato, L., Pannaccione, A., 2019. Amyloid  $\beta$ -Induced upregulation of Na v 1.6 underlies neuronal hyperactivity in Tg2576 Alzheimer's disease mouse model. *Sci. Rep.* 9, 13592. <https://doi.org/10.1038/s41598-019-50018-1>.
- Cohen, S.J., Stackman, R.W., 2015. Assessing rodent hippocampal involvement in the novel object recognition task. A review. *Behav. Brain Res.* 285, 105–117. <https://doi.org/10.1016/j.bbr.2014.08.002>.
- Cordella, A., Krashia, P., Nobili, A., Pignataro, A., La Barbera, L., Viscomi, M.T., Valzania, A., Keller, F., Ammassari-Teule, M., Mercuri, N.B., Berretta, N., D'Amelio, M., 2018. Dopamine loss alters the hippocampus-nucleus accumbens synaptic transmission in the Tg2576 mouse model of Alzheimer's disease. *Neurobiol. Dis.* 116, 142–154. <https://doi.org/10.1016/j.nbd.2018.05.006>.
- Corsetti, V., Borreca, A., Latina, V., Giacomazzo, G., Pignataro, A., Krashia, P., Natale, F., Cocco, S., Rinaudo, M., Malerba, F., Florio, R., Ciarapica, R., Coccorello, R., D'Amelio, M., Ammassari-Teule, M., Grassi, C., Calissano, P., Amadoro, G., 2020. Passive immunotherapy for N-truncated tau ameliorates the cognitive deficits in two mouse Alzheimer's disease models. *Brain Commun.* 2, 1–34. <https://doi.org/10.1093/braincomms/fcaa039>.
- Costa, C., Parnetti, L., D'Amelio, M., Tozzi, A., Tantucci, M., Romigi, A., Siliquini, S., Cavallucci, V., Di Filippo, M., Mazzocchetti, P., Liguori, C., Nobili, A., Eusebi, P., Mercuri, N.B., Calabresi, P., 2016. Epilepsy, amyloid- $\beta$ , and D1 dopamine receptors: a possible pathogenetic link? *Neurobiol. Aging* 48, 161–171. <https://doi.org/10.1016/j.neurobiolaging.2016.08.025>.
- Cutuli, D., De Bartolo, P., Caporali, P., Laricchiuta, D., Foti, F., Ronci, M., Rossi, C., Neri, C., Spalletta, G., Caltagirone, C., Farioli-Vecchioli, S., Petrosini, L., 2014. n-3 polyunsaturated fatty acids supplementation enhances hippocampal functionality in aged mice. *Front. Aging Neurosci.* 6, 220. <https://doi.org/10.3389/fnagi.2014.00220>.
- D'Amelio, M., Rossini, P.M., 2012. Brain excitability and connectivity of neuronal assemblies in Alzheimer's disease: from animal models to human findings. *Prog. Neurobiol.* 99, 42–60. <https://doi.org/10.1016/j.pneurobio.2012.07.001>.
- D'Amelio, M., Puglisi-Allegra, S., Mercuri, N., 2018a. The role of dopaminergic midbrain in Alzheimer's disease: translating basic science into clinical practice. *Pharmacol. Res.* 130, 414–419. <https://doi.org/10.1016/j.phrs.2018.01.016>.
- D'Amelio, M., Serra, L., Bozzali, M., 2018b. Ventral tegmental area in prodromal Alzheimer's disease: bridging the gap between mice and humans. *J. Alzheimers Dis.* 63, 181–183. <https://doi.org/10.3233/JAD-180094>.
- De Duve, C., Wattiaux, R., 1966. Functions of lysosomes. *Annu. Rev. Physiol.* 28, 435–492. <https://doi.org/10.1146/annurev.ph.28.030166.002251>.
- De Marco, M., Venneri, A., 2018. Volume and connectivity of the Ventral Tegmental Area are linked to neurocognitive signatures of Alzheimer's disease in humans. *J. Alzheimers Dis.* 63, 167–180. <https://doi.org/10.3233/JAD-171018>.
- Deremer, D.L., Ustun, C., Natarajan, K., 2008. Nilotinib: a second-generation tyrosine kinase inhibitor for the treatment of chronic myelogenous leukemia. *Clin. Ther.* 30, 1956–1975. <https://doi.org/10.1016/j.clinthera.2008.11.014>.
- Engel, D., Seutin, V., 2015. High dendritic expression of Ih in the proximity of the axon origin controls the integrative properties of nigral dopamine neurons. *J. Physiol. (Paris)* 593, 4905–4922. <https://doi.org/10.1113/JP271052>.
- Eskelinen, E.-L., 2008. To be or not to be? Examples of incorrect identification of autophagic compartments in conventional transmission electron microscopy of mammalian cells. *Autophagy* 4, 257–260. <https://doi.org/10.4161/auto.5179>.
- Gasbarri, A., Verney, C., Innocenzi, R., Campana, C., Pacitti, C., 1994. Mesolimbic dopaminergic neurons innervating the hippocampal formation in the rat: a combined retrograde tracing and immunohistochemical study. *Brain Res.* 668, 71–79. [https://doi.org/10.1016/0006-8993\(94\)90512-6](https://doi.org/10.1016/0006-8993(94)90512-6).
- Gasselin, C., Inglebert, Y., Debanne, D., 2015. Homeostatic regulation of h-conductance controls intrinsic excitability and stabilizes the threshold for synaptic modification in CA1 neurons. *J. Physiol. (Paris)* 593, 4855–4869. <https://doi.org/10.1113/JP271369>.
- Gerenu, G., Dobarro, M., Ramirez, M.J., Gil-Bea, F.J., 2013. Early cognitive stimulation compensates for memory and pathological changes in Tg2576 mice. *Biochim. Biophys. Acta* 1832, 837–847. <https://doi.org/10.1016/j.bbadis.2013.02.018>.
- Gibb, W.R., Mountjoy, C.Q., Mann, D.M., Lees, A.J., 1989. The substantia nigra and ventral tegmental area in Alzheimer's disease and Down's syndrome. *J. Neurol. Neurosurg. Psychiatry* 52, 193–200. <https://doi.org/10.1136/jnnp.52.2.193>.
- Giguère, N., Burke Nanni, S., Trudeau, L.-E., 2018. On cell loss and selective vulnerability of neuronal populations in parkinson's disease. *Front. Neurol.* 455, 9. <https://doi.org/10.3389/fneur.2018.00455>.
- Gonfloni, S., Maiani, E., Di Bartolomeo, C., Diederich, M., Cesareni, G., 2012. Oxidative stress, DNA damage, and c-Abl signaling: At the crossroad in neurodegenerative diseases? *Int. J. Cell Biol.* 2012, 683097. <https://doi.org/10.1155/2012/683097>.
- Guérin, D., Sacquet, J., Mandairon, N., Jourdan, F., Didier, A., 2009. Early locus coeruleus degeneration and olfactory dysfunction in Tg2576 mice. *Neurobiol. Aging* 30, 272–283. <https://doi.org/10.1016/j.neurobiolaging.2007.05.020>.
- Guzmán-Ramos, K., Moreno-Castilla, B., Castro-Cruz, M., McGaugh, J.L., Martínez-Coria, H., LaFerla, F.M., Bermúdez-Rattoni, F., 2012. Restoration of dopamine release deficits during object recognition memory acquisition attenuates cognitive impairment in a triple transgenic mouse model of Alzheimer's disease. *Learn. Mem.* 19, 453–460. <https://doi.org/10.1101/lm.026070.112>.
- Hao, J.-R., Sun, N., Lei, L., Li, X.-Y., Yao, B., Sun, K., Hu, R., Zhang, X., Shi, X.-D., Gao, C., 2015. L-Stepholidine rescues memory deficit and synaptic plasticity in models of Alzheimer's disease via activating dopamine D1 receptor/PKA signaling pathway. *Cell Death Dis.* 6, e1965. <https://doi.org/10.1038/cddis.2015.315>.
- Hardy, J., Selkoe, D.J., 2002. The amyloid hypothesis of Alzheimer's disease: progress and problems on the road to therapeutics. *Science* 297, 353–356. <https://doi.org/10.1126/science.1072994>.
- He, C., Chen, F., Li, B., Hu, Z., 2014. Neurophysiology of HCN channels: from cellular functions to multiple regulations. *Prog. Neurobiol.* 112, 1–23. <https://doi.org/10.1016/j.pneurobio.2013.10.001>.
- Hebron, M.L., Lonskaya, I., Moussa, C.E.-H., 2013a. Nilotinib reverses loss of dopamine neurons and improves motor behavior via autophagic degradation of  $\alpha$ -synuclein in Parkinson's disease models. *Hum. Mol. Genet.* 22, 3315–3328. <https://doi.org/10.1093/hmg/ddt192>.
- Hebron, M.L., Lonskaya, I., Sharpe, K., Weerasinghe, P.P.K., Algarzae, N.K., Shekoyan, A.R., Moussa, C.E.-H., 2013b. Parkin ubiquitinates Tar-DNA binding protein-43 (TDP-43) and promotes its cytosolic accumulation via interaction with histone deacetylase 6 (HDAC6). *J. Biol. Chem.* 288, 4103–4115. <https://doi.org/10.1074/jbc.M112.419945>.
- Hebron, M.L., Lonskaya, I., Olopade, P., Selby, S.T., Pagan, F., Moussa, C.E.-H., 2014. Tyrosine kinase inhibition regulates early systemic immune changes and modulates the neuroimmune response in  $\alpha$ -Synucleinopathy. *J. Clin. Cell. Immunol.* 5, 259. <https://doi.org/10.4172/2155-9899.1000259>.
- Hebron, M.L., Javidnia, M., Moussa, C.E.-H., 2018. Tau clearance improves astrocytic function and brain glutamate-glutamine cycle. *J. Neurol. Sci.* 391, 90–99. <https://doi.org/10.1016/j.jns.2018.06.005>.
- Henny, P., Brown, M.T.C., Northrop, A., Faunes, M., Ungless, M.A., Magill, P.J., Bolam, J.P., 2012. Structural correlates of heterogeneous in vivo activity of midbrain dopaminergic neurons. *Nat. Neurosci.* 15, 613–619. <https://doi.org/10.1038/nn.3048>.
- Herrup, K., 2015. The case for rejecting the amyloid cascade hypothesis. *Nat. Neurosci.* 18, 794–799. <https://doi.org/10.1038/nn.4017>.
- Himeno, E., Ohyagi, Y., Ma, L., Nakamura, N., Miyoshi, K., Sakae, N., Motomura, K., Soejima, N., Yamasaki, R., Hashimoto, T., Tabira, T., LaFerla, F.M., Kira, J., 2011. Apomorphine treatment in Alzheimer mice promoting amyloid- $\beta$  degradation. *Ann. Neurol.* 69, 248–256. <https://doi.org/10.1002/ana.22319>.
- Hsiao, K., Chapman, P., Nilsen, S., Eckman, C., Harigaya, Y., Younkin, S., Yang, F., Cole, G., 1996. Correlative memory deficits, A $\beta$  elevation, and amyloid plaques in transgenic mice. *Science* 274, 99–102. <https://doi.org/10.1126/science.274.5284.99>.
- Huang, Z., Lujan, R., Kadurin, I., Uebele, V.N., Renger, J.J., Dolphin, A.C., Shah, M.M., 2011. Presynaptic HCN1 channels regulate Cav3.2 activity and neurotransmission at select cortical synapses. *Nat. Neurosci.* 14, 478–486. <https://doi.org/10.1038/nn.2757>.
- Huang, L.-K., Chao, S.-P., Hu, C.-J., 2020. Clinical trials of new drugs for Alzheimer disease. *J. Biomed. Sci.* 27, 18. <https://doi.org/10.1186/s12929-019-0609-7>.
- Hunn, B.H.M., Vingill, S., Threlfell, S., Alegre-Abarrategui, J., Magdelyns, M., Deltheil, T., Bengoa-Vergniory, N., Oliver, P.L., Cioroch, M., Doig, N.M., Bannerman, D.M., Cragg, S.J., Wade-Martins, R., 2019. Impairment of

- macroautophagy in dopamine neurons has opposing effects on parkinsonian pathology and behavior. *Cell Rep.* 29, 920–931. <https://doi.org/10.1016/j.celrep.2019.09.029> e7.
- Iaccarino, L., Sala, A., Caminiti, S.P., Presotto, L., Perani, D., Alzheimer's Disease Neuroimaging Initiative, 2020. In vivo MRI structural and PET metabolic connectivity study of dopamine pathways in alzheimer's disease. *J. Alzheimers Dis.* 75, 1003–1016. <https://doi.org/10.3233/JAD-190954>.
- Imam, S.Z., Zhou, Q., Yamamoto, A., Valente, A.J., Ali, S.F., Bains, M., Roberts, J.L., Kahle, P.J., Clark, R.A., Li, S., 2011. Novel regulation of parkin function through c-Abl-mediated tyrosine phosphorylation: implications for Parkinson's disease. *J. Neurosci.* 31, 157–163. <https://doi.org/10.1523/JNEUROSCI.1833-10.2011>.
- Isidoro, C., Biagioni, F., Giorgi, F.S., Fulceri, F., Paparelli, A., Fornai, F., 2009. The role of autophagy on the survival of dopamine neurons. *Curr. Top. Med. Chem.* 9, 869–879. <https://doi.org/10.2174/156802609789378281>.
- Ismail, Z., Smith, E.E., Geda, Y., Sultzer, D., Brodaty, H., Smith, G., Agüera-Ortiz, L., Sweet, R., Miller, D., Lyketsos, C.G., ISTAART Neuropsychiatric Symptoms Professional Interest Area, 2016. Neuropsychiatric symptoms as early manifestations of emergent dementia: provisional diagnostic criteria for mild behavioral impairment. *Alzheimers Dement.* 12, 195–202. <https://doi.org/10.1016/j.jalz.2015.05.017>.
- Iyer, R., Ungless, M.A., Faisal, A.A., 2017. Calcium-activated SK channels control firing regularity by modulating sodium channel availability in midbrain dopamine neurons. *Sci. Rep.* 7, 5248. <https://doi.org/10.1038/s41598-017-05578-5>.
- Jessberger, S., Clark, R.E., Broadbent, N.J., Clemenson, G.D., Consiglio, A., Lie, D.C., Squire, L.R., Gage, F.H., 2009. Dentate gyrus-specific knockdown of adult neurogenesis impairs spatial and object recognition memory in adult rats. *Learn. Mem. Cold Spring Harb. N* 16, 147–154. <https://doi.org/10.1101/m.1172609>.
- Ji, H., Shepard, P.D., 2006. SK Ca<sup>2+</sup>-activated K<sup>+</sup> channel ligands alter the firing pattern of dopamine-containing neurons in vivo. *Neuroscience* 140, 623–633. <https://doi.org/10.1016/j.neuroscience.2006.02.020>.
- Ji, H., Hougaard, C., Herrik, K.F., Strøbaek, D., Christophersen, P., Shepard, P.D., 2009. Tuning the excitability of midbrain dopamine neurons by modulating the Ca<sup>2+</sup> sensitivity of SK channels. *Eur. J. Neurosci.* 29, 1883–1895. <https://doi.org/10.1111/j.1460-9568.2009.06735.x>.
- Jiang, Y.-M., Yamamoto, M., Kobayashi, Y., Yoshihara, T., Liang, Y., Terao, S., Takeuchi, H., Ishigaki, S., Katsuno, M., Adachi, H., Niwa, J.-I., Tanaka, F., Doyu, M., Yoshida, M., Hashizume, Y., Sobue, G., 2005. Gene expression profile of spinal motor neurons in sporadic amyotrophic lateral sclerosis. *Ann. Neurol.* 57, 236–251. <https://doi.org/10.1002/ana.20379>.
- Jing, Z., Caltagarone, J., Bowser, R., 2009. Altered subcellular distribution of c-Abl in Alzheimer's disease. *J. Alzheimers Dis.* 17, 409–422. <https://doi.org/10.3233/JAD-2009-1062>.
- Joyce, J.N., Smutzer, G., Whitty, C.J., Myers, A., Bannon, M.J., 1997. Differential modification of dopamine transporter and tyrosine hydroxylase mRNAs in midbrain of subjects with Parkinson's, Alzheimer's with parkinsonism, and Alzheimer's disease. *Mov. Disord.* 12, 885–897. <https://doi.org/10.1002/mds.870120609>.
- Jürgensen, S., Antonio, L.L., Mussi, G.E.A., Brito-Moreira, J., Bomfim, T.R., De Felice, F. G., Garrido-Sanabria, E.R., Cavalheiro, É.A., Ferreira, S.T., 2011. Activation of D1/D5 dopamine receptors protects neurons from synapse dysfunction induced by amyloid-beta oligomers. *J. Biol. Chem.* 286, 3270–3276. <https://doi.org/10.1074/jbc.M110.177790>.
- Karuppagounder, S.S., Brahmachari, S., Lee, Y., Dawson, V.L., Dawson, T.M., Ko, H.S., 2014. The c-Abl inhibitor, nilotinib, protects dopaminergic neurons in a preclinical animal model of Parkinson's disease. *Sci. Rep.* 4, 4874. <https://doi.org/10.1038/srep04874>.
- Kempadoo, K.A., Mosharov, E.V., Choi, S.J., Sulzer, D., Kandel, E.R., 2016. Dopamine release from the locus coeruleus to the dorsal hippocampus promotes spatial learning and memory. *Proc. Natl. Acad. Sci. U. S. A.* 113, 14835–14840. <https://doi.org/10.1073/pnas.1616515114>.
- Kempainen, N., Laine, M., Laakso, M.P., Kaasinen, V., Nägren, K., Vahlberg, T., Kurki, T., Rinne, J.O., 2003. Hippocampal dopamine D2 receptors correlate with memory functions in Alzheimer's disease. *Eur. J. Neurosci.* 18, 149–154. <https://doi.org/10.1046/j.1460-9568.2003.02716.x>.
- Klionsky, D.J., et al., 2021. Guidelines for the use and interpretation of assays for monitoring autophagy (4th edition). *Autophagy*. <https://doi.org/10.1080/15548627.2020.1797280>.
- Ko, H.S., Lee, Y., Shin, J.-H., Karuppagounder, S.S., Gadad, B.S., Koleske, A.J., Pletnikova, O., Troncoso, J.C., Dawson, V.L., Dawson, T.M., 2010. Phosphorylation by the c-Abl protein tyrosine kinase inhibits parkin's ubiquitination and protective function. *Proc. Natl. Acad. Sci. U. S. A.* 107, 16691–16696. <https://doi.org/10.1073/pnas.1006083107>.
- Koch, G., Esposito, Z., Codecà, C., Mori, F., Kusayanagi, H., Monteleone, F., Di Lorenzo, F., Bernardi, G., Martorana, A., 2011. Altered dopamine modulation of LTD-like plasticity in Alzheimer's disease patients. *Clin. Neurophysiol.* 122, 703–707. <https://doi.org/10.1016/j.clinph.2010.10.033>.
- Koch, G., Di Lorenzo, F., Bonni, S., Giacobbe, V., Bozzali, M., Caltagirone, C., Martorana, A., 2014. Dopaminergic modulation of cortical plasticity in Alzheimer's disease patients. *Neuropsychopharmacology* 39, 2654–2661. <https://doi.org/10.1038/npp.2014.119>.
- Koch, G., Motta, C., Bonni, S., Pellicciari, M.C., Picazio, S., Casula, E.P., Maiella, M., Di Lorenzo, F., Ponzio, V., Ferrari, C., Scaricamazza, E., Caltagirone, C., Martorana, A., 2020. Effect of rotigotine vs placebo on cognitive functions among patients with mild to moderate alzheimer disease: a randomized clinical trial. *JAMA Netw. Open* 3, e2010372. <https://doi.org/10.1001/jamanetworkopen.2020.10372>.
- Koyama, S., Appel, S.B., 2006. Characterization of M-current in ventral tegmental area dopamine neurons. *J. Neurophysiol.* 96, 535–543. <https://doi.org/10.1152/jn.00574.2005>.
- Krashia, P., Martini, A., Nobili, A., Aversa, D., D'Amelio, M., Berretta, N., Guatteo, E., Mercuri, N.B., 2017. On the properties of identified dopaminergic neurons in the mouse substantia nigra and ventral tegmental area. *Eur. J. Neurosci.* 45, 92–105. <https://doi.org/10.1111/ejn.13364>.
- Krashia, P., Cordella, A., Nobili, A., La Barbera, L., Federici, M., Leuti, A., Campanelli, F., Natale, G., Marino, G., Calabrese, V., Vedele, F., Ghiglieri, V., Picconi, B., Di Lazzaro, G., Schirinzi, T., Sancesario, G., Casadei, N., Riess, O., Bernardini, S., Pisani, A., Calabresi, P., Viscomi, M.T., Serhan, C.N., Chiurchiù, V., D'Amelio, M., Mercuri, N.B., 2019a. Blunting neuroinflammation with resolvin D1 prevents early pathology in a rat model of Parkinson's disease. *Nat. Commun.* 10, 3945. <https://doi.org/10.1038/s41467-019-11928-w>.
- Krashia, P., Nobili, A., D'Amelio, M., 2019b. Unifying hypothesis of dopamine neuron loss in neurodegenerative diseases: focusing on alzheimer's disease. *Front. Neurosci.* 12. <https://doi.org/10.3389/fnmol.2019.00123>.
- Kumar, U., Patel, S.C., 2007. Immunohistochemical localization of dopamine receptor subtypes (D1R-D5R) in Alzheimer's disease brain. *Brain Res.* 1131, 187–196. <https://doi.org/10.1016/j.brainres.2006.10.049>.
- Lammel, S., Hetzel, A., Häckel, O., Jones, I., Liss, B., Roeper, J., 2008. Unique properties of mesoprefrontal neurons within a dual mesocorticolimbic dopamine system. *Neuron* 57, 760–773. <https://doi.org/10.1016/j.neuron.2008.01.022>.
- Latini, L., Bisicchia, E., Sasso, V., Chiurchiù, V., Cavallucci, V., Molinari, M., Maccarrone, M., Viscomi, M.T., 2014. Cannabinoid CB2 receptor (CB2R) stimulation delays subspinal mitochondrial-dependent degeneration and improves functional recovery after spinal cord hemisection by ERK1/2 inactivation. *Cell Death Dis.* 5, e1404. <https://doi.org/10.1038/cddis.2014.364>.
- Lieberman, O.J., Frier, M.D., McGuirt, A.F., Griffey, C.J., Rafikian, E., Yang, M., Yamamoto, A., Borgkvist, A., Santini, E., Sulzer, D., 2020. Cell-type-specific regulation of neuronal intrinsic excitability by macroautophagy. *eLife* e50843. <https://doi.org/10.7554/eLife.50843>, 9.
- Lindholm, D., Pham, D.D., Cascone, A., Eriksson, O., Wennerberg, K., Saarma, M., 2016. C-abl inhibitors enable insights into the pathophysiology and neuroprotection in parkinson's disease. *Front. Aging Neurosci.* 254, 8. <https://doi.org/10.3389/fnagi.2016.00254>.
- Lisman, J.E., Grace, A.A., 2005. The hippocampal-VTA loop: controlling the entry of information into long-term memory. *Neuron* 46, 703–713. <https://doi.org/10.1016/j.neuron.2005.05.002>.
- Liu, Y., Yoo, M.-J., Savonenko, A., Stirling, W., Price, D.L., Borchelt, D.R., Mamounas, L., Lyons, W.E., Blue, M.E., Lee, M.K., 2008. Amyloid pathology is associated with progressive monoaminergic neurodegeneration in a transgenic mouse model of Alzheimer's disease. *J. Neurosci.* 28, 13805–13814. <https://doi.org/10.1523/JNEUROSCI.4218-08.2008>.
- Lonskaya, I., Desforges, N.M., Hebron, M.L., Moussa, C.E.-H., 2013a. Ubiquitination increases parkin activity to promote autophagic  $\alpha$ -synuclein clearance. *PLoS One* 8, e83914. <https://doi.org/10.1371/journal.pone.0083914>.
- Lonskaya, I., Hebron, M.L., Desforges, N.M., Franjie, A., Moussa, C.E.-H., 2013b. Tyrosine kinase inhibition increases functional parkin-Beclin-1 interaction and enhances amyloid clearance and cognitive performance. *EMBO Mol. Med.* 5, 1247–1262. <https://doi.org/10.1002/emmm.201302771>.
- Lonskaya, I., Hebron, M.L., Desforges, N.M., Schachter, J.B., Moussa, C.E.-H., 2014. Nilotinib-induced autophagic changes increase endogenous parkin level and ubiquitination, leading to amyloid clearance. *J. Mol. Med.* 92, 373–386. <https://doi.org/10.1007/s00109-013-1112-3>.
- Lonskaya, I., Hebron, M.L., Selby, S.T., Turner, R.S., Moussa, C.E.-H., 2015. Nilotinib and bosutinib modulate pre-plaque alterations of blood immune markers and neuroinflammation in Alzheimer's disease models. *Neuroscience* 304, 316–327. <https://doi.org/10.1016/j.neuroscience.2015.07.070>.
- Lyketsos, C.G., Carrillo, M.C., Ryan, J.M., Khachaturian, A.S., Trzepacz, P., Amatniek, J., Cedarbaum, J., Brashear, R., Miller, D.S., 2011. Neuropsychiatric symptoms in Alzheimer's disease. *Alzheimers Dement.* 7, 532–539. <https://doi.org/10.1016/j.jalz.2011.05.2410>.
- Mahon, F.-X., Hayette, S., Lagarde, V., Belloc, F., Turcq, B., Nicolini, F., Belanger, C., Manley, P.W., Leroy, C., Etienne, G., Roche, S., Pasquet, J.-M., 2008. Evidence that resistance to nilotinib may be due to BCR-ABL, Pgp, or Src kinase overexpression. *Cancer Res.* 68, 9809–9816. <https://doi.org/10.1158/0008-5472.CAN-08-1008>.
- Mahul-Mellier, A.-L., Fauvet, B., Gysbers, A., Dikiy, I., Oueslati, A., Georgeon, S., Lamontanara, A.J., Bisquert, A., Eliezer, D., Maslah, E., Halliday, G., Hantschel, O., Lashuel, H.A., 2014. c-Abl phosphorylates  $\alpha$ -synuclein and regulates its degradation: implication for  $\alpha$ -synuclein clearance and contribution to the pathogenesis of Parkinson's disease. *Hum. Mol. Genet.* 23, 2858–2879. <https://doi.org/10.1093/hmg/ddt674>.
- Mamad, O., Stumpp, L., McNamara, H.M., Ramakrishnan, C., Deisseroth, K., Reilly, R.B., Tsanov, M., 2017. Place field assembly distribution encodes preferred locations. *PLoS Biol.* 15, e2002365. <https://doi.org/10.1371/journal.pbio.2002365>.
- Margolis, E.B., Mitchell, J.M., Ishikawa, J., Hjelmstad, G.O., Fields, H.L., 2008. Midbrain dopamine neurons: projection target duration and dopamine D(2) receptor inhibition. *J. Neurosci.* 28, 8908–8913. <https://doi.org/10.1523/JNEUROSCI.1526-08.2008>.
- Martorana, A., Koch, G., 2014. Is dopamine involved in Alzheimer's disease? *Front. Aging Neurosci.* 6, 252. <https://doi.org/10.3389/fnagi.2014.00252>.
- Masi, A., Narducci, R., Resta, F., Carbone, C., Kobayashi, K., Mannaioni, G., 2015. Differential contribution of Ih to the integration of excitatory synaptic inputs in substantia nigra pars compacta and ventral tegmental area dopaminergic neurons. *Eur. J. Neurosci.* 42, 2699–2706. <https://doi.org/10.1111/ejn.13066>.

- Masters, M.C., Morris, J.C., Roe, C.M., 2015. "Nongenerative" symptoms of early Alzheimer disease: a longitudinal analysis. *Neurology* 84, 617–622. <https://doi.org/10.1212/WNL.0000000000001238>.
- Mathon, D.S., Kamal, A., Smidt, M.P., Ramakers, G.M.J., 2003. Modulation of cellular activity and synaptic transmission in the ventral tegmental area. *Eur. J. Pharmacol.* 480, 97–115. <https://doi.org/10.1016/j.ejphar.2003.08.097>.
- Matus, S., Valenzuela, V., Hetz, C., 2014. A new method to measure autophagy flux in the nervous system. *Autophagy* 10, 710–714. <https://doi.org/10.4161/auto.28434>.
- McCarthy, J.V., Cotter, T.G., 1997. Cell shrinkage and apoptosis: a role for potassium and sodium ion efflux. *Cell Death Differ.* 4, 756–770. <https://doi.org/10.1038/sj.cdd.4400296>.
- McNamara, C.G., Tejero-Cantero, Á., Trouche, S., Campo-Urriza, N., Dupret, D., 2014. Dopaminergic neurons promote hippocampal reactivation and spatial memory persistence. *Nat. Neurosci.* 17, 1658–1660. <https://doi.org/10.1038/nn.3843>.
- Melone, M., Ciriachi, C., Pietrobon, D., Conti, F., 2019. Heterogeneity of Astrocytic and neuronal GLT-1 at cortical excitatory synapses, as revealed by its colocalization with Na<sup>+</sup>/K<sup>+</sup>-ATPase  $\alpha$  isoforms. *Cereb. Cortex* 29, 3331–3350. <https://doi.org/10.1093/cercor/bhy203>.
- Mercuri, N.B., Bonci, A., Calabresi, P., Stefani, A., Bernardi, G., 1995. Properties of the hyperpolarization-activated cation current Ih in rat midbrain dopaminergic neurons. *Eur. J. Neurosci.* 7, 462–469. <https://doi.org/10.1111/j.1460-9568.1995.tb00342.x>.
- Monteverde, A., Gnemmi, P., Rossi, F., Monteverde, A., Finali, G.C., 1990. Selegiline in the treatment of mild to moderate Alzheimer-type dementia. *Clin. Ther.* 12, 315–322.
- Morales, M., Margolis, E.B., 2017. Ventral tegmental area: cellular heterogeneity, connectivity and behaviour. *Nat. Rev. Neurosci.* 18, 73–85. <https://doi.org/10.1038/nrn.2016.165>.
- Moreno-Castilla, P., Rodriguez-Duran, L.F., Guzman-Ramos, K., Barcenas-Femat, A., Escobar, M.L., Bermudez-Rattoni, F., 2016. Dopaminergic neurotransmission dysfunction induced by amyloid- $\beta$  transforms cortical long-term potentiation into long-term depression and produces memory impairment. *Neurobiol. Aging* 41, 187–199. <https://doi.org/10.1016/j.neurobiolaging.2016.02.021>.
- Murphy, M.J.M., Deutch, A.Y., 2018. Organization of afferents to the orbitofrontal cortex in the rat. *J. Comp. Neurol.* 526, 1498–1526. <https://doi.org/10.1002/cne.24424>.
- Murray, A.M., Weihmueller, F.B., Marshall, J.F., Hurtig, H.I., Gottlieb, G.L., Joyce, J.N., 1995. Damage to dopamine systems differs between Parkinson's disease and Alzheimer's disease with parkinsonism. *Ann. Neurol.* 37, 300–312. <https://doi.org/10.1002/ana.410370306>.
- Musiek, E.S., Bhimasani, M., Zangrilli, M.A., Morris, J.C., Holtzman, D.M., Ju, Y.-E.S., 2018. Circadian rest-activity pattern changes in aging and preclinical Alzheimer disease. *JAMA Neurol.* 75, 582–590. <https://doi.org/10.1001/jamaneurol.2017.4719>.
- Neuhoff, H., Neu, A., Liss, B., Roeper, J., 2002. I(h) channels contribute to the different functional properties of identified dopaminergic subpopulations in the midbrain. *J. Neurosci.* 22, 1290–1302. <https://doi.org/10.1523/JNEUROSCI.22-04-01290.2002>.
- Nixon, R.A., 2013. The role of autophagy in neurodegenerative disease. *Nat. Med.* 19, 983–997. <https://doi.org/10.1038/nm.3232>.
- Nixon, R.A., Cataldo, A.M., 2006. Lysosomal system pathways: genes to neurodegeneration in Alzheimer's disease. *J. Alzheimers Dis.* 9, 277–289. <https://doi.org/10.3233/jad-2006-9s331>.
- Nixon, R.A., Wegiel, J., Kumar, A., Yu, W.H., Peterhoff, C., Cataldo, A., Cuervo, A.M., 2005. Extensive involvement of autophagy in Alzheimer disease: an immunoelectron microscopy study. *J. Neuropathol. Exp. Neurol.* 64, 113–122. <https://doi.org/10.1093/jnen/64.2.113>.
- Nobili, A., Cavallucci, V., D'Amelio, M., 2016. Role of autophagy in brain sculpture: physiological and pathological implications. In: Maiuri, M.C., De Stefano, D. (Eds.), *Autophagy Networks in Inflammation, Progress in Inflammation Research*. Springer International Publishing, Cham, pp. 203–234. [https://doi.org/10.1007/978-3-319-30079-5\\_11](https://doi.org/10.1007/978-3-319-30079-5_11).
- Nobili, A., Latagliata, E.C., Viscomi, M.T., Cavallucci, V., Cutuli, D., Giacobuzzo, G., Krashia, P., Rizzo, F.R., Marino, R., Federici, M., De Bartolo, P., Aversa, D., Dell'Acqua, M.C., Cordella, A., Sancandi, M., Keller, F., Petrosini, L., Pugliese-Allegra, S., Mercuri, N.B., Coccurello, R., Berretta, N., D'Amelio, M., 2017. Dopamine neuronal loss contributes to memory and reward dysfunction in a model of Alzheimer's disease. *Nat. Commun.* 8, 14727. <https://doi.org/10.1038/ncomms14727>.
- Nobili, A., Krashia, P., Cordella, A., La Barbera, L., Dell'Acqua, M.C., Caruso, A., Pignataro, A., Marino, R., Sciarra, F., Biamonte, F., Scattoni, M.L., Ammassari-Teule, M., Cecconi, F., Berretta, N., Keller, F., Mercuri, N.B., D'Amelio, M., 2018. Ambra1 shapes hippocampal Inhibition/Excitation balance: role in neurodevelopmental disorders. *Mol. Neurobiol.* 55, 7921–7940. <https://doi.org/10.1007/s12035-018-0911-5>.
- Noebels, J.L., 2011. A perfect storm: converging paths of epilepsy and Alzheimer's dementia intersect in the hippocampal formation. *Epilepsia* 52, 39–46. <https://doi.org/10.1111/j.1528-1167.2010.02909.x>.
- Pagan, F., Hebron, M., Valadez, E.H., Torres-Yaghi, Y., Huang, X., Mills, R.R., Wilmarth, B.M., Howard, H., Dunn, C., Carlson, A., Lawler, A., Rogers, S.L., Falconer, R.A., Ahn, J., Li, Z., Moussa, C., 2016. Nilotinib effects in parkinson's disease and dementia with Lewy bodies. *J. Park. Dis.* 6, 503–517. <https://doi.org/10.3233/JPD-160867>.
- Pagan, F.L., Hebron, M.L., Wilmarth, B., Torres-Yaghi, Y., Lawler, A., Mundel, E.E., Yusuf, N., Starr, N.J., Anjum, M., Arellano, J., Howard, H.H., Shi, W., Mulki, S., Kurd-Misto, T., Matar, S., Liu, X., Ahn, J., Moussa, C., 2019. Nilotinib effects on safety, tolerability, and potential biomarkers in parkinson disease: a phase 2 randomized clinical trial. *JAMA Neurol.* 77, 309–317. <https://doi.org/10.1001/jamaneurol.2019.4200>.
- Paxinos, G., Franklin, K., 2012. *The Mouse Brain in Stereotaxic Coordinates*, 4th ed. Elsevier/Academic Press.
- Pazini, A.M., Gomes, G.M., Villarinho, J.G., da Cunha, C., Pinheiro, F., Ferreira, A.P.O., Mello, C.F., Ferreira, J., Rubin, M.A., 2013. Selegiline reverses  $\alpha\beta$ -induced cognitive deficit in male mice. *Neurochem. Res.* 38, 2287–2294. <https://doi.org/10.1007/s11064-013-1137-6>.
- Peters, A., Palay, S.L., Webster, Hde F., 1991. *The Fine Structure of the Nervous System: Neurons and Their Supporting Cells*, 3rd ed. OUP USA, New York, ed.
- Phend, K.D., Rustioni, A., Weinberg, R.J., 1995. An osmium-free method of epon embedment that preserves both ultrastructure and antigenicity for post-embedding immunocytochemistry. *J. Histochem. Cytochem.* 43, 283–292. <https://doi.org/10.1177/43.3.7532656>.
- Rinne, J.O., Säkö, E., Paljärvi, L., Mölsä, P.K., Rinne, U.K., 1986a. Brain dopamine D-1 receptors in senile dementia. *J. Neurol. Sci.* 73, 219–230. [https://doi.org/10.1016/0022-510x\(86\)90132-2](https://doi.org/10.1016/0022-510x(86)90132-2).
- Rinne, J.O., Säkö, E., Paljärvi, L., Mölsä, P.K., Rinne, U.K., 1986b. Brain dopamine D-2 receptors in senile dementia. *J. Neural Transm.* 65, 51–62. <https://doi.org/10.1007/bf01249611>.
- Roeper, J., 2013. Dissecting the diversity of midbrain dopamine neurons. *Trends Neurosci.* 36, 336–342. <https://doi.org/10.1016/j.tins.2013.03.003>.
- Rosen, Z.B., Cheung, S., Siegelbaum, S.A., 2015. Midbrain dopamine neurons bidirectionally regulate CA3-CA1 synaptic drive. *Nat. Neurosci.* 18, 1763–1771. <https://doi.org/10.1038/nn.4152>.
- Rossato, J.I., Bevilacqua, L.R.M., Izquierdo, I., Medina, J.H., Cammarota, M., 2009. Dopamine controls persistence of long-term memory storage. *Science* 325, 1017–1020. <https://doi.org/10.1126/science.1172545>.
- Sato, S., Uchiyama, T., Fukuda, T., Noda, S., Kondo, H., Saiki, S., Komatsu, M., Uchiyama, Y., Tanaka, K., Hattori, N., 2018. Loss of autophagy in dopaminergic neurons causes Lewy pathology and motor dysfunction in aged mice. *Sci. Rep.* 8, 2813. <https://doi.org/10.1038/s41598-018-21325-w>.
- Schlatterer, S.D., Acker, C.M., Davies, P., 2011. C-abl in neurodegenerative disease. *J. Mol. Neurosci.* 45, 445–452. <https://doi.org/10.1007/s12031-011-9588-1>.
- Serra, L., D'Amelio, M., Di Domenico, C., Dipasquale, O., Marra, C., Mercuri, N.B., Caltagirone, C., Cercignani, M., Bozzali, M., 2018. In vivo mapping of brainstem nuclei functional connectivity disruption in Alzheimer's disease. *Neurobiol. Aging* 72, 72–82. <https://doi.org/10.1016/j.neurobiolaging.2018.08.012>.
- Seutin, V., Massotte, L., Renette, M.F., Dresse, A., 2001. Evidence for a modulatory role of Ih on the firing of a subgroup of midbrain dopamine neurons. *Neuroreport* 12, 255–258. <https://doi.org/10.1097/00001756-200102120-00015>.
- Skorski, T., 2011. BCR-ABL1 kinase: hunting an elusive target with new weapons. *Chem. Biol.* 18, 1352–1353. <https://doi.org/10.1016/j.chembiol.2011.11.001>.
- Son, S.M., Jung, E.S., Shin, H.J., Byun, J., Mook-Jung, I., 2012.  $\alpha\beta$ -induced formation of autophagosomes is mediated by RAGE- CamKK $\beta$ -AMPK signaling. *Neurobiol. Aging* 33 (1006), e11–23. <https://doi.org/10.1016/j.neurobiolaging.2011.09.039>.
- Squire, L.R., Wixted, J.T., Clark, R.E., 2007. Recognition memory and the medial temporal lobe: a new perspective. *Nat. Rev. Neurosci.* 8, 872–883. <https://doi.org/10.1038/nrn2154>.
- Storga, D., Vrecko, K., Birkmayer, J.G., Reibnegger, G., 1996. Monoaminergic neurotransmitters, their precursors and metabolites in brains of Alzheimer patients. *Neurosci. Lett.* 203, 29–32. [https://doi.org/10.1016/0304-3940\(95\)12256-7](https://doi.org/10.1016/0304-3940(95)12256-7).
- Subramaniam, M., Althof, D., Gispert, S., Schwenk, J., Auburger, G., Kulik, A., Fakler, B., Roeper, J., 2014. Mutant  $\alpha$ -Synuclein enhances firing frequencies in dopamine substantia nigra neurons by oxidative impairment of A-Type potassium channels. *J. Neurosci.* 34, 13586–13599. <https://doi.org/10.1523/JNEUROSCI.5069-13.2014>.
- Sulzer, D., 2007. Multiple hit hypotheses for dopamine neuron loss in Parkinson's disease. *Trends Neurosci.* 30, 244–250. <https://doi.org/10.1016/j.tins.2007.03.009>.
- Tagliavola, G., Hogan, D., Zhang, W.-R., Dineley, K.T., 2009. Intermediate- and long-term recognition memory deficits in Tg2576 mice are reversed with acute calcineurin inhibition. *Behav. Brain Res.* 200, 95–99. <https://doi.org/10.1016/j.bbr.2008.12.034>.
- Takeuchi, T., Duszkiewicz, A.J., Sonneborn, A., Spooner, P.A., Yamasaki, M., Watanabe, M., Smith, C.C., Fernández, G., Deisseroth, K., Greene, R.W., Morris, R.G.M., 2016. Locus coeruleus and dopaminergic consolidation of everyday memory. *Nature* 537, 357–362. <https://doi.org/10.1038/nature19325>.
- Tanida, I., Minematsu-Ikeguchi, N., Ueno, T., Kominami, E., 2005. Lysosomal turnover, but not a cellular level, of endogenous LC3 is a marker for autophagy. *Autophagy* 1, 84–91. <https://doi.org/10.4161/auto.1.2.1697>.
- Tanzi, R.E., Bertram, L., 2005. Twenty years of the Alzheimer's disease amyloid hypothesis: a genetic perspective. *Cell* 120, 545–555. <https://doi.org/10.1016/j.cell.2005.02.008>.
- Ting, J.T., Lee, B.R., Chong, P., Soler-Llavina, G., Cobbs, C., Koch, C., Zeng, H., Lein, E., 2018. Preparation of acute brain slices using an optimized N-Methyl-D-glucamine protective recovery method. *J. Vis. Exp.* 53825. <https://doi.org/10.3791/53825>.
- Tremblay, M.A., Acker, C.M., Davies, P., 2010. Tau phosphorylated at tyrosine 394 is found in Alzheimer's disease tangles and can be a product of the Abl-related kinase. *Arg. J. Alzheimers Dis.* 19, 721–733. <https://doi.org/10.3233/JAD-2010-1271>.
- Tsunekawa, H., Noda, Y., Mouri, A., Yoneda, F., Nabeshima, T., 2008. Synergistic effects of selegiline and donepezil on cognitive impairment induced by amyloid beta (25–35). *Behav. Brain Res.* 190, 224–232. <https://doi.org/10.1016/j.bbr.2008.03.002>.
- Turner, R.S., Hebron, M.L., Lawler, A., Mundel, E.E., Yusuf, N., Starr, J.N., Anjum, M., Pagan, F., Torres-Yaghi, Y., Shi, W., Mulki, S., Ferrante, D., Matar, S., Liu, X., Esposito, G., Berkowitz, F., Jiang, X., Ahn, J., Moussa, C., 2020. Nilotinib effects on safety, tolerability, and biomarkers in Alzheimer's disease. *Ann. Neurol.* 88, 183–194. <https://doi.org/10.1002/ana.25775>.

- Venneri, A., De Marco, M., 2020. Reduced monoaminergic nuclei MRI signal detectable in pre- symptomatic older adults with future memory decline. *Sci. Rep.* 10, 18707. <https://doi.org/10.1038/s41598-020-71368-1>.
- Viscomi, M.T., D'Amelio, M., 2012. The "Janus- Faced role" of autophagy in neuronal sickness: focus on neurodegeneration. *Mol. Neurobiol.* 46, 513–521. <https://doi.org/10.1007/s12035-012-8296-3>.
- Waroux, O., Massotte, L., Alleva, L., Graulich, A., Thomas, E., Liégeois, J.-F., Scuvée-Moreau, J., Seutin, V., 2005. SK channels control the firing pattern of midbrain dopaminergic neurons in vivo. *Eur. J. Neurosci.* 22, 3111–3121. <https://doi.org/10.1111/j.1460-9568.2005.04484.x>.
- White, F.J., 1996. Synaptic regulation of mesocorticolimbic dopamine neurons. *Annu. Rev. Neurosci.* 19, 405–436. <https://doi.org/10.1146/annurev.ne.19.030196.002201>.
- Yang, D.-S., Stavrides, P., Mohan, P.S., Kaushik, S., Kumar, A., Ohno, M., Schmidt, S.D., Wesson, D., Bandyopadhyay, U., Jiang, Y., Pawlik, M., Peterhoff, C.M., Yang, A.J., Wilson, D.A., St George-Hyslop, P., Westaway, D., Mathews, P.M., Levy, E., Cuervo, A.M., Nixon, R.A., 2011. Reversal of autophagy dysfunction in the TgCRND8 mouse model of Alzheimer's disease ameliorates amyloid pathologies and memory deficits. *Brain* 134, 258–277. <https://doi.org/10.1093/brain/awq341>.
- Yang, K., Broussard, J.L., Levine, A.T., Jenson, D., Arenkiel, B.R., Dani, J.A., 2017. Dopamine receptor activity participates in hippocampal synaptic plasticity associated with novel object recognition. *Eur. J. Neurosci.* 45, 138–146. <https://doi.org/10.1111/ejn.13406>.
- Yang, H., de Jong, J.W., Tak, Y., Peck, J., Bateup, H., Lammel, S., 2018. Nucleus accumbens subnuclei regulate motivated behavior via direct inhibition and disinhibition of VTA dopamine subpopulations. *Neuron* 97, 434–449. <https://doi.org/10.1016/j.neuron.2017.12.022> e4.
- Ylä-Anttila, P., Vihinen, H., Jokitalo, E., Eskelinen, E.-L., 2009. Monitoring autophagy by electron microscopy in Mammalian cells. *Methods Enzymol.* 452, 143–164. [https://doi.org/10.1016/S0076-6879\(08\)03610-0](https://doi.org/10.1016/S0076-6879(08)03610-0).
- Yu, W.H., Cuervo, A.M., Kumar, A., Peterhoff, C.M., Schmidt, S.D., Lee, J.-H., Mohan, P. S., Mercken, M., Farmery, M.R., Tjernberg, L.O., Jiang, Y., Duff, K., Uchiyama, Y., Näslund, J., Mathews, P.M., Cataldo, A.M., Nixon, R.A., 2005. Macroautophagy—a novel Beta-amyloid peptide-generating pathway activated in Alzheimer's disease. *J. Cell Biol.* 171, 87–98. <https://doi.org/10.1083/jcb.200505082>.
- Zhang, T.A., Placzek, A.N., Dani, J.A., 2010. In vitro identification and electrophysiological characterization of dopamine neurons in the Ventral Tegmental Area. *Neuropharmacology* 59, 431–436. <https://doi.org/10.1016/j.neuropharm.2010.06.004>.
- Zhou, F., van Laar, T., Huang, H., Zhang, L., 2011. APP and APLP1 are degraded through autophagy in response to proteasome inhibition in neuronal cells. *Protein Cell* 2, 377–383. <https://doi.org/10.1007/s12328-011-1047-9>.